J. Fluid Mech. (2004), *vol.* 500, *pp.* 169–210.
DOI: 10.1017/S0022112003007158 Printed in the United Kingdom

Stability of circular Poiseuille–Couette flow to axisymmetric disturbances

By ANDREW G. WALTON

Department of Mathematics, Imperial College London,
South Kensington Campus, London SW7 2AZ, UK

(Received 19 May 2003 and in revised form 11 September 2003)

The stability of circular Poiseuille–Couette flow to axisymmetric disturbances is investigated theoretically. First, the governing circular Orr–Sommerfeld equation for linear perturbations is formulated and analysed asymptotically at large values of the Reynolds number. The existence of multiple regions of instability is predicted and their dependence upon radius ratio and inner cylinder velocity is determined explicitly. These findings are confirmed when the linear problem is solved numerically at finite Reynolds number and multiple neutral curves are found. The relevance of these results to the thread injection of medical implants is discussed, and it is shown how the linear modes are connected to nonlinear amplitude-dependent modes at high Reynolds number that exist for $O(1)$ values of the inner cylinder velocity.

1. Introduction and formulation of the governing equations

1.1. *Preliminary discussion*

The linear stability of the exact Navier–Stokes solution representing the axial-pressure-gradient-driven flow through a cylindrical annulus (circular Poiseuille–Couette flow) was first considered by Mott & Joseph (1968). They studied the case where the inner cylinder is at rest and the disturbances are axisymmetric in nature. Neutral curves (along which the growth rate of the disturbance is zero) were generated in the Reynolds number–axial wavenumber plane for various values of the radius ratio δ of the inner to the outer cylinder. It was found that there is a monotonic increase in critical Reynolds number (based on gap width and maximum velocity) with decreasing δ. There appears to have been little further significant activity on this problem until the numerical study of Sadeghi & Higgins (1991). In the latter paper, the inner cylinder is taken to move in the axial direction with a prescribed constant speed V, and stability to both axisymmetric and non-symmetric disturbances for a range of values of V and δ is considered numerically. For every choice of the parameters that they investigated, Sadeghi & Higgins produced a unique neutral curve. They also discovered that these curves retreated to infinity at a finite value of V (the 'cutoff' velocity), dependent upon δ (and the azimuthal wavenumber for non-symmetric disturbances).

The proposal of a unique neutral curve for non-zero values of V was somewhat surprising as an earlier asymptotic study of plane Poiseuille–Couette flow by Cowley & Smith (1985), and numerical studies carried out by the present author, suggest that in the two-dimensional problem multiple neutral curves do coexist. This was then confirmed in the circular case by the numerical work of Gittler (1993) for axisymmetric disturbances. He found the existence of two neutral curves at non-zero

V for the particular configuration $\delta = 0.5$, in contradiction with the results of Sadeghi & Higgins. One of the aims of the present work is to see whether asymptotic analysis of the disturbance equations can lead to a prediction of the range of values of V and δ over which multiple neutral curves exist and to an understanding of the physical processes involved in the curve splitting.

Recently, there has been some renewed interest in this flow as it is relevant to the 'thread injection' of medical implants (Frei, Lüscher & Wintermantel 2000; Walton 2003). It was while working on this application that the present author decided that a revisiting of the linear stability problem was in order. In fact, the stability properties of this flow turn out to be so intricate that we confine ourselves in this paper to a full account of the axisymmetric problem. We begin by analysing the linear stability equations asymptotically at high Reynolds number R. There are three main reasons for adopting this approach: (i) the stability equations are stiff at large R and numerical results can often be at best unreliable; (ii) an asymptotic approach (Cowley & Smith 1985) proved fruitful for plane Poiseuille–Couette flow; (iii) an analysis for $R \gg 1$ will provide us with a knowledge of the crucial values of V and δ at which multiple neutral curves exist, and this will serve as an all-important guide when carrying out finite-Reynolds-number calculations.

The asymptotic study is presented in § 2. The approach we adopt and the scalings we obtain are similar to those of Cowley & Smith, although the present problem is a little more involved owing to the cylindrical geometry and the more complicated basic flow. The main ideas remain the same, however, but we present our analysis in more detail than the aforementioned authors, because their main interest centred on how the disturbances behaved at $O(1)$ values of V, whereas here all the asymptotic results are found to be relevant when it comes to computing neutral curves at finite Reynolds number in § 3. It is convenient to fix the radius ratio in these computations and investigate how the neutral stability curve(s) for a given geometry change as V is increased. Although we recover the neutral curves of Sadeghi & Higgins, we find a great deal more besides: there are indeed multiple neutral curves (confirming the results of Gittler 1993), sometimes co-existing at relatively low Reynolds number with their shape (including whether they are open or closed) depending crucially on the values of the parameters δ and V. We discuss the results and their relevance to the medical application more fully in § 4, where it is also shown how they are connected to nonlinear neutral modes as the disturbance amplitude is increased.

In the remainder of this section we introduce our notation and formulate the linear stability problem.

1.2. *The governing equations, non-dimensionalization and basic flow*

The cylindrical polar coordinate system (a^*x, a^*r, θ) is used throughout this paper where x, r and θ represent the non-dimensional coordinates in the axial, radial and azimuthal directions, respectively, with a^* the radius of the outer cylinder. Our focus here is on axisymmetric flows with no swirl and the (x, r) velocity components are written as $(g^*a^{*2}/\rho^*\nu^*)(u, v)$ where $-4g^*$ is the constant axial pressure gradient applied to the flow through the annulus. The pressure is expressed as $(g^{*2}a^{*4}/\rho^*\nu^{*2})p$ where ρ^* is the density of the incompressible fluid and ν^* is its kinematic viscosity. The time is written in the form $(\rho^*\nu^*/g^*a^*)t$. These scalings enable us to pose the governing unsteady axisymmetric Navier–Stokes equations in the non-dimensional form:

$$\nabla \cdot \boldsymbol{u} = 0, \quad \boldsymbol{u}_t + (\boldsymbol{u} \cdot \nabla)\boldsymbol{u} = -\nabla p + R^{-1}\nabla^2 \boldsymbol{u}, \quad R = g^*a^{*3}/\rho^*\nu^{*2}, \quad \boldsymbol{u} = (u, v). \tag{1.1}$$

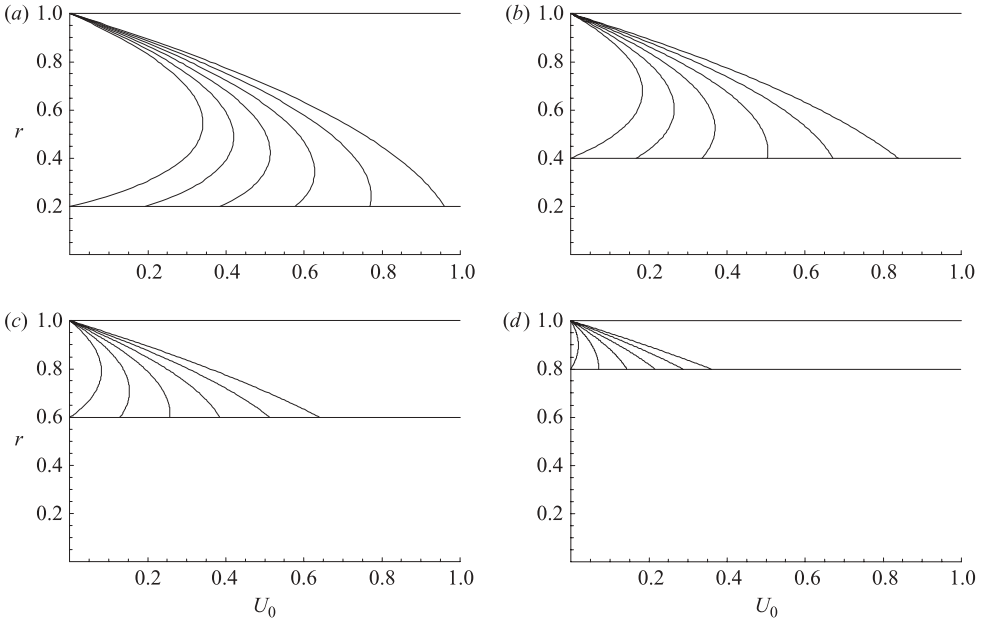

FIGURE 1. The basic Poiseuille–Couette flow $U_0(r)$ for various values of inner cylinder velocity V and radius δ. (*a*) $\delta = 0.2$; (*b*) $\delta = 0.4$; (*c*) $\delta = 0.6$; (*d*) $\delta = 0.8$. In each case, six equally spaced values of V are shown ranging from (left to right) $V = 0$ to $V = 1 - \delta^2$.

Note that other forms of non-dimensionalization are possible: for instance we could base the Reynolds number upon flux or on maximum velocity (as in Sadeghi & Higgins 1991). However, the fixed pressure gradient case is the most relevant for the thread injection application and that is the main motivation for our choice here.

Our basic state is the axial flow between concentric cylinders with $r = 1$ representing the outer surface and $r = \delta$ the inner surface. The inner cylinder is moving in the axial direction with non-dimensional velocity V (corresponding to the dimensional velocity $V^* = (g^* a^{*2}/\rho^* \nu^*)V$). We seek a steady, unidirectional solution $\boldsymbol{u} = (U_0(r), 0)$ to the Navier–Stokes equations (1.1), and find

$$U_0 = 1 - r^2 + \frac{(V - 1 + \delta^2)}{\ln \delta} \ln r \quad (\delta \leqslant r \leqslant 1). \tag{1.2}$$

In this paper we study the linear and nonlinear stability of this basic solution for various values of V and δ. Sketches of the basic flow for a range of the parameters are shown in figure 1. We will concentrate on $V > 0$ as this is the regime of interest for medical applications, but we will indicate later how the analysis is altered when $V < 0$.

1.3. *Formulation of the axisymmetric linear disturbance equations*

A small axisymmetric travelling-wave disturbance of non-dimensional amplitude Δ is superimposed upon the basic flow and is expressed as the real part of

$$\Delta(\widehat{u}(r), \widehat{v}(r), \widehat{p}(r)) \exp(\mathrm{i}\alpha(x - ct)). \tag{1.3}$$

We will adopt a temporal approach to the stability problem, allowing the wavespeed c to be complex, while the axial wavenumber α is required to be real. The governing equations for the disturbance are obtained by adding the perturbation to the basic

flow, substituting into (1.1) and equating coefficients of Δ, leading to the following set of linear equations:

$$\mathrm{i}\alpha\hat{u} + \hat{v}' + \hat{v}/r = 0, \tag{1.4a}$$

$$\mathrm{i}\alpha(U_0 - c)\hat{u} + \hat{v}U_0' = -\mathrm{i}\alpha\hat{p} + R^{-1}(\hat{u}'' + \hat{u}'/r - \alpha^2\hat{u}), \tag{1.4b}$$

$$\mathrm{i}\alpha(U_0 - c)\hat{v} = -\hat{p}' + R^{-1}(\hat{v}'' + \hat{v}'/r - \hat{v}/r^2 - \alpha^2\hat{v}), \tag{1.4c}$$

subject to the no-slip boundary conditions

$$\hat{u} = \hat{v} = 0 \text{ on } r = \delta, r = 1. \tag{1.5}$$

The pressure $\hat{p}$ and streamwise perturbation $\hat{u}$ can be eliminated, leaving the disturbance governed by the following cylindrical version of the Orr–Sommerfeld equation (where $\phi = r\hat{v}$):

$$\begin{aligned}(U_0 - c)(\phi'' - \phi'/r - \alpha^2\phi) - (U_0'' - U_0'/r)\phi \\ = (\mathrm{i}\alpha R)^{-1}(\phi^{\mathrm{iv}} - 2\phi'''/r + (3/r^2 - 2\alpha^2)\phi'' + (2\alpha^2/r - 3/r^3)\phi' + \alpha^4\phi),\end{aligned} \tag{1.6}$$

with the boundary conditions $\phi = \phi' = 0$ on $r = \delta$, $r = 1$. The latter form of the equation is convenient for the numerical approach adopted in §§ 2.4 and 3, while the primitive form (1.4) is useful for a high-Reynolds-number asymptotic approach (§ 2.2).

2. The solution of the linear stability equations at large Reynolds number

The solution of (1.6) for given values of V and δ is a numerical one in general, but some analytical progress can be made by assuming that the Reynolds number is large. As mentioned above, the asymptotic analysis is not performed as an alternative to numerical computation, but rather to complement it. First, in this section we consider the inviscid limit of (1.6) before considering the viscous instability at high Reynolds number.

2.1. *Inviscid instability*

When $R = \infty$, the Orr–Sommerfeld equation reduces to its Rayleigh counterpart, namely

$$(U_0 - c)\left(\frac{\mathrm{d}}{\mathrm{d}r}\left(\frac{\phi'}{\alpha^2 r}\right) - \frac{\phi}{r}\right) - \frac{\mathrm{d}}{\mathrm{d}r}\left(\frac{U_0'}{\alpha^2 r}\right)\phi = 0. \tag{2.1}$$

The analogous result to Rayleigh's inflection point criterion can be obtained by multiplying by $\phi^*/(U_0 - c)$ (with $*$ denoting complex conjugate), integrating across the annulus, and applying the no-slip boundary conditions. We find that

$$c_i \int_\delta^1 \left(\frac{\mathrm{d}}{\mathrm{d}r}\left(\frac{U_0'}{\alpha^2 r}\right)\frac{|\phi|^2}{|U_0 - c|^2}\right)\mathrm{d}r = 0, \tag{2.2}$$

where c_i denotes the imaginary part of c. Thus, inviscid instability is only possible if $(U_0'/\alpha^2 r)'$ changes sign somewhere in the range $\delta \leqslant r \leqslant 1$. It is easy to show that for the basic flow (1.2) this quantity is, in fact, constant and therefore inviscid stability is assured. Incidentally, this argument can also be extended to show that the flow is also inviscidly stable to non-axisymmetric disturbances; in such cases α^2 is replaced by $\alpha^2 + N^2/r^2$, where N is the azimuthal wavenumber of the disturbance.

Now that we have established that any linear instability of (1.2) is viscous in nature, we consider the viscous problem at high Reynolds number.

2.2. *Viscous instability*

As the Reynolds number is assumed large, viscous effects will be confined to the proximity of the cylindrical walls. It is therefore useful to give here the near-wall behaviour of the basic flow for small values of V. Letting $V = \varepsilon^2 V_0$, we have

$$U_0 = U_{00} + \varepsilon^2 U_{01}, \quad U_{00} = 1 - r^2 - (1-\delta^2)\frac{\ln r}{\ln \delta}, \quad U_{01} = V_0 \frac{\ln r}{\ln \delta}. \tag{2.3}$$

As $r \to 1-$:

$$U_{00} \sim \lambda_+^{(0)}(1-r) + \lambda_+^{(10)}(1-r)^2, \quad U_{01} \sim \lambda_+^{(1)}(1-r), \tag{2.4}$$

with

$$\lambda_+^{(0)} = 2 + \frac{(1-\delta^2)}{\ln \delta} > 0, \quad \lambda_+^{(10)} = -1 + \frac{(1-\delta^2)}{2\ln \delta} < 0, \quad \lambda_+^{(1)} = -\frac{V_0}{\ln \delta} > 0.$$

As $r \to \delta +$:

$$U_{00} \sim \lambda_-^{(0)}(r-\delta) + \lambda_-^{(10)}(r-\delta)^2, \quad U_{01} \sim V_0 + \lambda_-^{(1)}(r-\delta), \tag{2.5}$$

with

$$\lambda_-^{(0)} = -2\delta - \frac{(1-\delta^2)}{\delta \ln \delta} > 0, \quad \lambda_-^{(10)} = -1 + \frac{(1-\delta^2)}{2\delta^2 \ln \delta} < 0, \quad \lambda_-^{(1)} = \frac{V_0}{\delta \ln \delta} < 0.$$

These forms will come in useful at various points in the analysis.

2.2.1. *Lower-branch analysis*

When $V = 0$, by analogy with the corresponding stability analysis for other parallel flows and from previous numerical studies, we anticipate that there will be a unique neutral stability curve. Typically, on the lower branch of such a curve at high Reynolds number, the two critical layers (where the basic flow is equal to the phase speed c of the disturbance) will be embedded within viscous wall layers and we anticipate that the mode behaviour will be described by a three-zone structure consisting of a core region and two wall layers. A sketch of the asymptotic structure is shown in figure 2. If V is non-zero, but less than or of the same magnitude as c, we would expect this structure to remain essentially intact and so we seek an asymptotic solution to (1.4) of this form when $R \gg 1$ and

$$V = \varepsilon^2 V_0, \quad \varepsilon \ll 1,$$

with ε to be determined in terms of the Reynolds number.

(i) *Core region I.* Here the basic flow is much larger than the wavespeed of the perturbation and the dynamics are predominantly inviscid. The disturbance expansion, to leading order, is

$$\widehat{u} = F_0, \quad \widehat{v} = \varepsilon G_0, \quad \widehat{p} = \varepsilon^2 P_0, \quad \alpha = \varepsilon \alpha_0, \quad c = \varepsilon^2 c_0. \tag{2.6}$$

Substituting these expressions into the disturbance equations, with U_0 given by (2.3) we obtain a set of inviscid balances with solutions

$$F_0 = A_0 U_{00}'/r, \quad G_0 = -\mathrm{i}\alpha_0 A_0 U_{00}/r, \quad P_0 = \widehat{P}_0 + \alpha_0^2 A_0 I(r), \tag{2.7}$$

where the integral $I(r)$ is defined by

$$I(r) = \int_r^1 U_{00}^2/r \, \mathrm{d}r, \tag{2.8}$$

(and can be calculated analytically), while the constant A_0 is an undetermined amplitude factor. The pressure constant $\widehat{P}_0$ in (2.7) can be chosen without loss

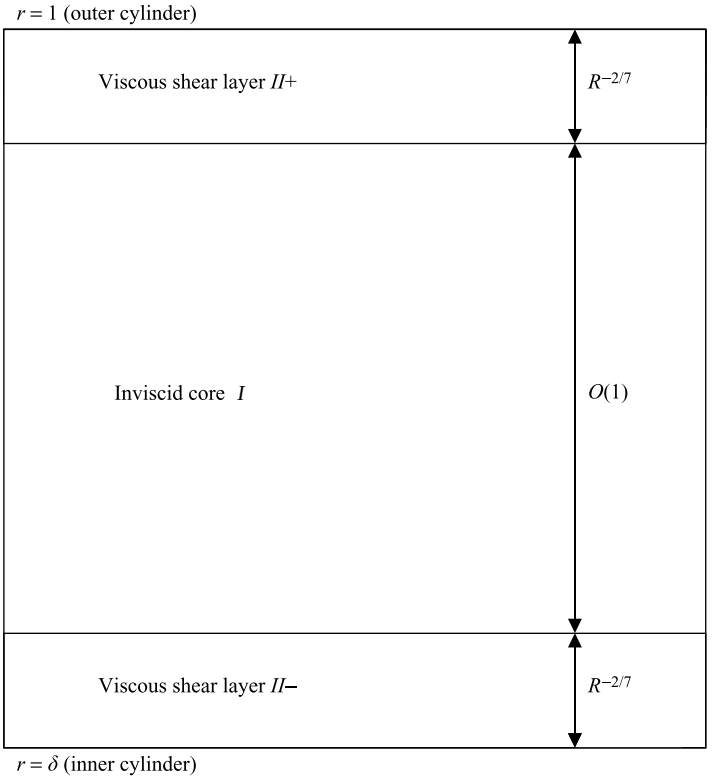

FIGURE 2. The high-Reynolds-number asymptotic structure of the lower-branch modes.

of generality and its value does not affect the eigenrelation to be derived below. Using the asymptotic forms (2.4), (2.5) for U_0 we see that as $r \to 1$:

$$F_0 \to -A_0\lambda_+^{(0)}, \quad G_0 \sim -\mathrm{i}\alpha_0 A_0 \lambda_+^{(0)}(1-r), \quad P_0 \to \widehat{P}_0, \tag{2.9}$$

while as $r \to \delta$:

$$F_0 \to A_0\lambda_-^{(0)}/\delta, \quad G_0 \sim -\mathrm{i}\alpha_0 A_0 \lambda_-^{(0)}(r-\delta)/\delta, \quad P_0 \to \widehat{P}_0 + \alpha_0^2 A_0 I(\delta). \tag{2.10}$$

(ii) *The inner viscous layers* $II+, II-$. In these regions (of thickness h say) the inertia term $\mathrm{i}\alpha(U_0 - c)\widehat{u}$, the pressure term $\mathrm{i}\alpha\widehat{p}$ and the viscous term $R^{-1}\widehat{u}''$ must all be comparable in size. This implies the balance

$$\varepsilon h \sim \varepsilon^3 \sim R^{-1}h^{-2},$$

resulting in the scalings

$$\varepsilon = R^{-1/7}, \quad \alpha = R^{-1/7}\alpha_0, \quad c = R^{-2/7}c_0, \quad V = R^{-2/7}V_0, \tag{2.11}$$

identical to those found for plane Poiseuille–Couette flow by Cowley & Smith (1985). The scaling of $R^{-2/7}$ in V allows the effects of the inner cylinder's motion to penetrate within the lower viscous layer ($II-$) at $r = \delta$. Having established the magnitude of the various parameters we can write down the equations governing the behaviour in the upper and lower viscous wall layers. In the upper layer ($II+$) we have to leading order

$$\widehat{u} = \overline{u}_+, \quad \widehat{v} = -\varepsilon^3\overline{v}_+, \quad \widehat{p} = \varepsilon^2\overline{p}_+, \quad r = 1 - \varepsilon^2\overline{y}_+, \quad U_0 = \varepsilon^2\lambda_+^{(0)}\overline{y}_+,$$

while in the lower layer ($II-$) the analogous expansions are

$$\widehat{u} = \overline{u}_-, \quad \widehat{v} = \varepsilon^3 \overline{v}_-, \quad \widehat{p} = \varepsilon^2 \overline{p}_-, \quad r = \delta + \varepsilon^2 \overline{y}_-, \quad U_0 = \varepsilon^2 \big(\lambda_-^{(0)} \overline{y}_- + V_0\big).$$

The corresponding equations and boundary conditions are

$$\mathrm{i}\alpha_0 \overline{u}_+ + \overline{v}'_+ = 0, \tag{2.12a}$$

$$\mathrm{i}\alpha_0 \big(\lambda_+^{(0)} \overline{y}_+ - c_0\big)\overline{u}_+ + \overline{v}_+ \lambda_+^{(0)} = -\mathrm{i}\alpha_0 \overline{p}_+ + \overline{u}''_+, \tag{2.12b}$$

$$\overline{p}_+ = \widehat{P}_0, \tag{2.12c}$$

$$\overline{u}_+ = \overline{v}_+ = 0 \text{ on } \overline{y}_+ = 0, \quad \overline{u}_+ \to -A_0 \lambda_+^{(0)} \text{ as } \overline{y}_+ \to \infty, \tag{2.12d}$$

in $II+$, and

$$\mathrm{i}\alpha_0 \overline{u}_- + \overline{v}'_- = 0, \tag{2.13a}$$

$$\mathrm{i}\alpha_0 \big(\lambda_-^{(0)} \overline{y}_- + V_0 - c_0\big)\overline{u}_- + \overline{v}_- \lambda_-^{(0)} = -\mathrm{i}\alpha_0 \overline{p}_- + \overline{u}''_-, \tag{2.13b}$$

$$\overline{p}_- = \widehat{P}_0 + \alpha_0^2 A_0 I(\delta), \tag{2.13c}$$

$$\overline{u}_- = \overline{v}_- = 0 \text{ on } \overline{y}_- = 0, \quad \overline{u}_- \to A_0 \lambda_-^{(0)}/\delta \text{ as } \overline{y}_- \to \infty, \tag{2.13d}$$

in $II-$ near the lower wall at $r = \delta$. The solutions for $\overline{p}_+$, $\overline{p}_-$ arise from the fact that the pressure is constant to leading order throughout both wall layers. The solution to these linear wall-layer problems is well known (e.g. Smith 1979) and leads us to the relations

$$\alpha_0^2 \overline{p}_+ = \big(\mathrm{i}\alpha_0 \lambda_+^{(0)}\big)^{5/3} \frac{\mathrm{Ai}'(\xi_+)}{\kappa(\xi_+)} A_0, \quad \alpha_0^2 \overline{p}_- = -\big(\mathrm{i}\alpha_0 \lambda_-^{(0)}\big)^{5/3} \frac{\mathrm{Ai}'(\xi_-)}{\delta \kappa(\xi_-)} A_0, \tag{2.14a, b}$$

where Ai is the Airy function, $\kappa(\xi) = \int_\xi^\infty \mathrm{Ai}(\xi)\,\mathrm{d}\xi$, and ξ_+, ξ_- are given by

$$(\xi_+, \xi_-) = -\mathrm{i}^{1/3}(s_+, s_-), \text{ with } s_+ = \frac{\alpha_0 c_0}{\big(\alpha_0 \lambda_+^{(0)}\big)^{2/3}}, \quad s_- = \frac{\alpha_0 (c_0 - V_0)}{\big(\alpha_0 \lambda_-^{(0)}\big)^{2/3}}. \tag{2.15}$$

We note that $s_+ > 0$, while s_- can be positive or negative. Subtracting (2.14*a*) from (2.14*b*), and using the expressions (2.12*c*), (2.13*c*) for $\overline{p}_+, \overline{p}_-$ we obtain the lower-branch eigenrelation

$$-\alpha_0^{7/3} I(\delta) = \big(\lambda_+^{(0)}\big)^{5/3} g(s_+) + \frac{1}{\delta}\big(\lambda_-^{(0)}\big)^{5/3} g(s_-), \tag{2.16}$$

where

$$g(s) = \mathrm{i}^{5/3} \mathrm{Ai}'(\xi)/\kappa(\xi), \quad \xi = -\mathrm{i}^{1/3} s. \tag{2.17}$$

In order to determine the possible neutral solutions for α_0 for given V_0 and δ it is necessary to solve (2.16) numerically. This is most easily accomplished by first eliminating the explicit α_0-dependence in the eigenrelation by noting that

$$\alpha_0^{1/3} V_0 = \big(\lambda_+^{(0)}\big)^{2/3} s_+ - \big(\lambda_-^{(0)}\big)^{2/3} s_-, \tag{2.18}$$

and using this expression to substitute for α_0. As a result, the eigenrelation becomes

$$V_0^7 \left(\big(\lambda_+^{(0)}\big)^{5/3} g(s_+) + \frac{1}{\delta}\big(\lambda_-^{(0)}\big)^{5/3} g(s_-) \right) + \left(\big(\lambda_+^{(0)}\big)^{2/3} s_+ - \big(\lambda_-^{(0)}\big)^{2/3} s_- \right)^7 I(\delta) = 0. \tag{2.19}$$

For given values of the parameters V_0 and δ, we can plot (as functions of s_+ and s_-) contours along which the real and imaginary parts of the left-hand side of (2.19) are zero. The intersection of these contours identifies the neutral values of s_+, s_- and hence determines the corresponding neutral values of α_0 from (2.18).

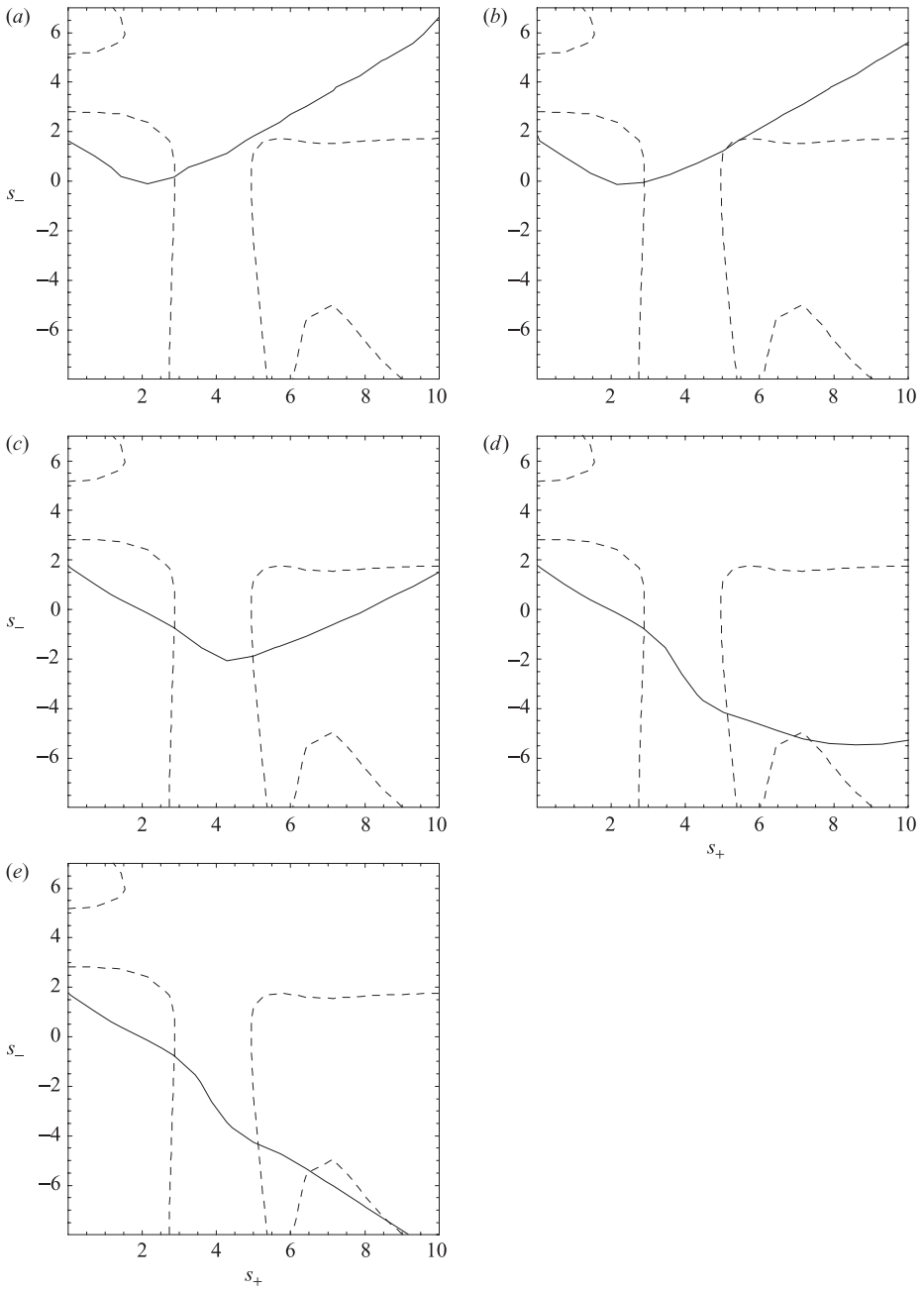

FIGURE 3. Solutions of the lower-branch eigenrelation (2.19) with $\delta = 0.95$ for various values of inner cylinder velocity V_0. (*a*) $V_0 = 0.08$; (*b*) $V_0 = 0.095$; (*c*) $V_0 = 0.2$; (*d*) $V_0 = 0.42$; (*e*) $V_0 = 5$. Along the dashed curves the imaginary part of the left-hand side of (2.19) is zero, while along the bold curves the real part is zero.

In figure 3 we show results for $\delta = 0.95$, and examine the contours as V_0 increases. When V_0 is in the range $0 \leqslant V_0 < 0.095$, there is just one intersection of the contours and hence one lower branch mode. When $V_0 \simeq 0.095$, two new modes form (figure 3*b*) and we see that as V_0 is further increased, one of these intersection points moves

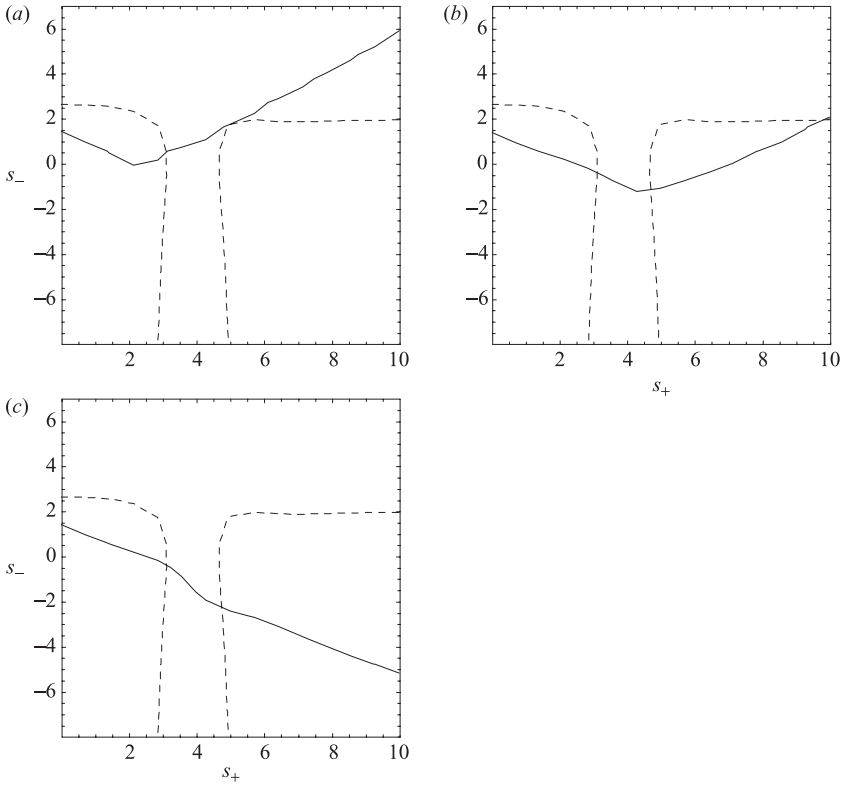

FIGURE 4. Solutions of the lower-branch eigenrelation (2.19) with $\delta = 0.7$ for: (*a*) $V_0 = 0.6$; (*b*) $V_0 = 1.4$; (*c*) $V_0 = 5$. Notation as in figure 3.

in such a way that $s_+ \to \infty$ as $V_0 \to \infty$, with s_- remaining finite and positive (i.e. $\alpha_0 \to \infty$), implying that the wavelength of this mode is shortening with increasing V. At around $V_0 \simeq 0.42$, a further two modes are created (figure 3*d*) and all four of these solutions persist as $V_0 \to \infty$. We now see how this sequence of events is modified when δ is decreased. Figure 4 shows the corresponding situation for $\delta = 0.7$. In this case, there is a unique solution until V_0 is increased to about 0.6 (figure 4*a*), at which point two new modes form. Once again, one of these modes shortens its wavelength as $V_0 \to \infty$. No further modes are created; in fact, we only observe the creation of the second pair of modes when $\delta \gtrsim 0.92$. Figure 5 shows the corresponding situation for $\delta = 0.4$. This time, only the $V_0 = 0$ mode exists (no other modes are created) with this mode shortening its wavelength as $V_0 \to \infty$. We found that this scenario was typical for the range $0 < \delta \lesssim 0.5$. It is already clear that the behaviour of the modes and their dependence upon the values of V and δ is a complicated issue. To help clarify the situation (and to determine the ultimate fate of these modes as V is increased) it is instructive to examine the eigenrelation (2.19) in the limit $V_0 \to \infty$. In this limit (assuming that s_+ and s_- remain $O(1)$), it is clear that the eigenrelation simplifies to

$$\left(\lambda_+^{(0)}\right)^{5/3} g(s_+) + \frac{1}{\delta}\left(\lambda_-^{(0)}\right)^{5/3} g(s_-) \simeq 0. \tag{2.20}$$

Figure 6 shows the corresponding contours for selected values of δ between 0.95 and 0.4. These results reinforce the conclusions drawn above, namely that in the limit $V_0 \to \infty$ we have four such solutions for $0.92 < \delta < 1$, two solutions for $0.52 < \delta < 0.92$, and no solutions for $\delta < 0.52$. These modes all have a wavelength which is increasing,

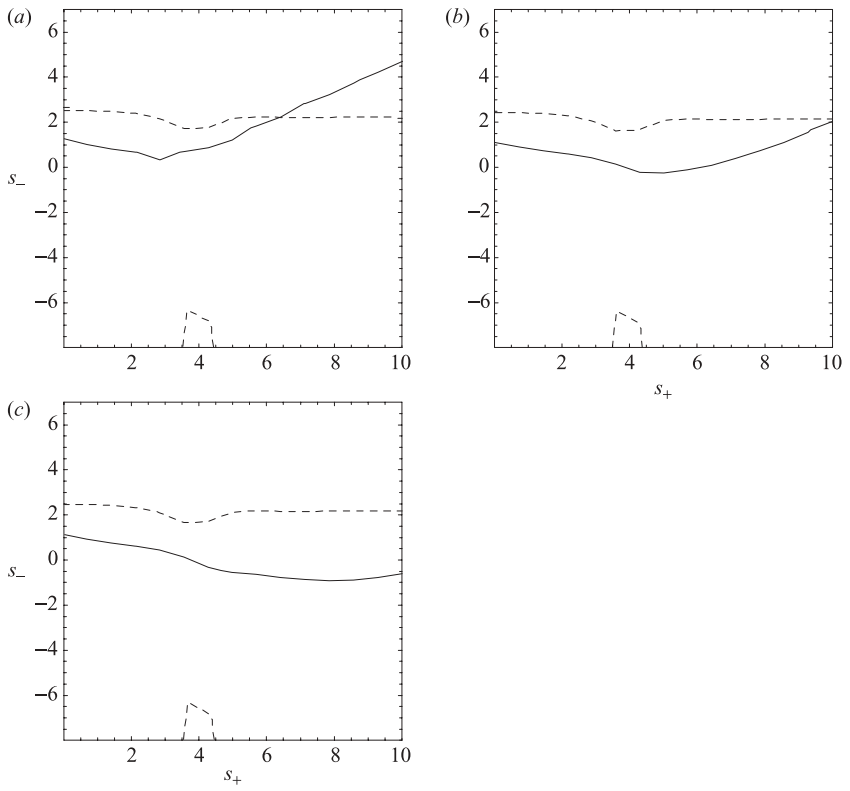

FIGURE 5. Solutions of the lower-branch eigenrelation (2.19) with $\delta = 0.4$ for: (*a*) $V_0 = 1.5$; (*b*) $V_0 = 3$; (*c*) $V_0 = 5$. Notation as in figure 3.

according to

$$\alpha_0 \sim \left(\left(\lambda_+^{(0)}\right)^{2/3} s_+ - \left(\lambda_-^{(0)}\right)^{2/3} s_- \right)^3 V_0^{-3} \text{ as } V_0 \to \infty, \tag{2.21}$$

from (2.18). In addition to these solutions, we also have the solution for which $s_+ \to \infty$ with s_- remaining $O(1)$ as $V_0 \to \infty$. It can be shown that in this limit

$$g(s) \sim -s + \mathrm{e}^{\mathrm{i}\pi/4} s^{-1/2} \text{ as } s \to \infty. \tag{2.22}$$

Thus, to leading order $g(s_+)$ is real and therefore $g(s_-)$ must also be real to balance the terms in (2.19). This is only possible if

$$s_- = s_0 \simeq 2.2972, \tag{2.23}$$

the unique (finite) root of $\mathrm{Im}(g) = 0$. After substitution for s_+ from (2.15) the appropriate limiting form of the eigenrelation (2.19) is found to be

$$-\alpha_0^{7/3} I(\delta) \sim -\lambda_+^{(0)} \left(\left(\lambda_-^{(0)}\right)^{2/3} s_0 + \alpha_0^{1/3} V_0 \right) + \frac{1}{\delta} \left(\lambda_-^{(0)}\right)^{5/3} g(s_0). \tag{2.24}$$

Upon rearrangement, we obtain the result

$$V_0 \sim \left(I(\delta) / \lambda_+^{(0)} \right) \alpha_0^2 + O\left(\alpha_0^{-1/3}\right) \quad \text{as } V_0 \to \infty. \tag{2.25}$$

This demonstrates explicitly how this mode shortens its wavelength as V_0 is increased. In view of the fact that for this mode the quantity s_- remains $O(1)$ and positive, it is

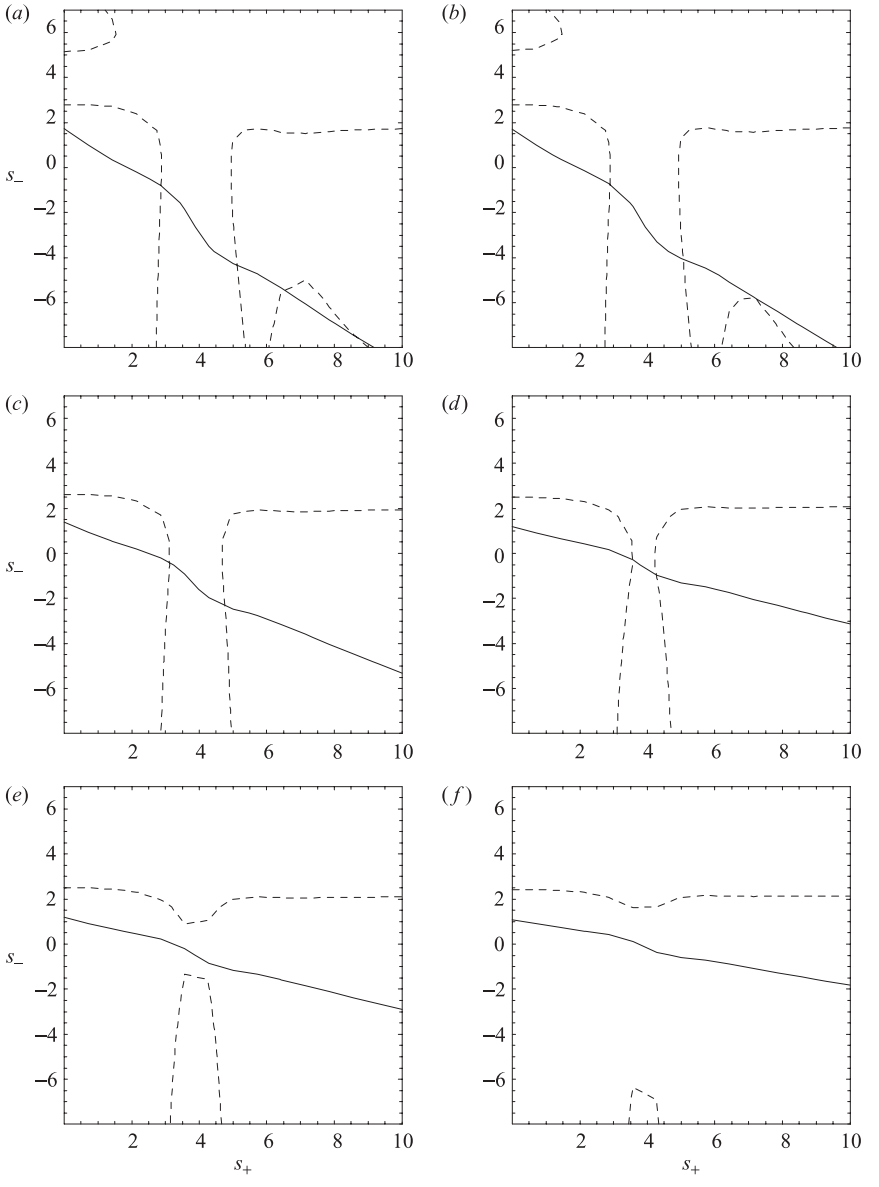

FIGURE 6. Solutions of the lower-branch eigenrelation (2.20) for asymptotically large V_0, for the following values of δ: (*a*) 0.95; (*b*) 0.92; (*c*) 0.7; (*d*) 0.52; (*e*) 0.5; (*f*) 0.4. Along the dashed curves the imaginary part of the left-hand side of (2.20) is zero, while along the bold curves the real part is zero.

evident that the wavespeed also increases, with

$$c_0 \sim V_0 + \left(\frac{\lambda_+^{(0)}}{I(\delta)}\right)^{-1/6} \left(\lambda_-^{(0)}\right)^{2/3} s_0 V_0^{-1/6} \quad \text{as } V_0 \to \infty, \tag{2.26}$$

from (2.15), (2.25). For this mode, as V increases, the critical layer is moving away from the upper wall, while the lower critical layer remains embedded within its viscous layer. Thus, the upper part of the structure is turning into an upper-branch-type mode

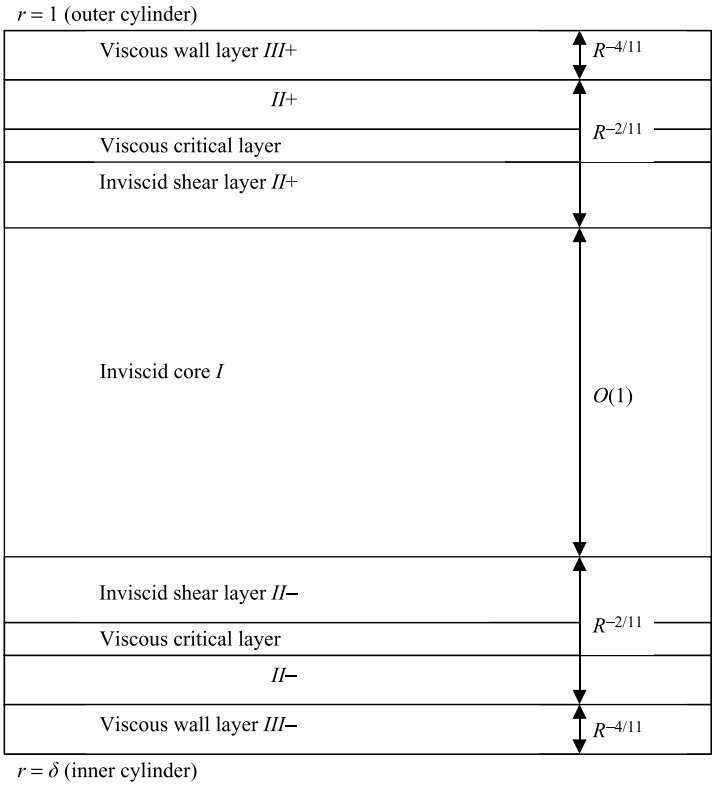

FIGURE 7. The nine zone asymptotic structure of the upper-branch mode.

while the lower part still retains the lower-branch structure. We will investigate this hybrid mode further in § 2.2.3.

Thus, as $V_0 \to \infty$ we have two types of mode. The first type has a wavelength that increases as V_0 increases. The number of such solutions is either four, two or none depending on the value of δ. For these modes, the critical layers remain embedded within the viscous wall layers and the asymptotic structure remains intact until V_0 increases to order $R^{2/7}$ (i.e. V becomes $O(1)$). From the asymptotic behaviour (2.21) and the scaling (2.11), we see that in this limit the disturbance wavelength increases to $O(R)$, at which stage the further evolution with V becomes a numerical problem (to be tackled in § 2.4). The second type of mode (of which there is always one for all values of δ) has a wavelength which decreases as V_0 increases, and behaves according to (2.25). We will see later that the structure associated with this mode breaks down before V becomes $O(1)$, although this can be extended by including nonlinear effects. Before we can study this mode further it is necessary to examine the structure of the upper-branch mode at small values of V.

2.2.2. *Upper-branch analysis*

The aim here is to set out the structure of the upper-branch mode for this flow when the inner cylinder velocity is small and to identify the distinguished scaling for V, beyond which this structure breaks down. The distinguishing feature of the upper-branch behaviour is that the typical value of the disturbance wavespeed is larger than that on the lower branch and as a result the critical layers are distinct from the viscous wall layers. This leads to a nine-zone structure formally (sketched in figure 7).

The structure is not quite as complicated as it may first appear, however, as eight of these regions occur in upper wall/lower wall pairs (denoted by $+/-$ subscripts). As in the lower-branch case, there is an inviscid core region (I) in which the basic flow velocity is much larger than the disturbance wavespeed. This is surrounded above and below by an inviscid shear layer (regions $II+, II-$), in which the basic near-wall shear flow is of the same order of magnitude as the wavespeed. The viscous critical layers (required to smooth out the singularities in $II+, II-$) are sited within their respective shear layers. Finally, in order that the disturbance satisfies no-slip on both cylinders, we require viscous wall layers ($III+, III-$). Once again, we seek a solution with $V \ll 1$, $R \gg 1$ and write

$$V = \varepsilon^2 V_0, \quad U_0 = U_{00} + \varepsilon^2 U_{01},$$

(with U_{00}, U_{01} given in (2.3)). The small parameter ε is again to be determined in terms of the Reynolds number.

(i) *Inviscid core region I.* First, we consider the core region where the dynamics are exactly as in the lower-branch case. It is necessary, however, to calculate higher-order terms in the expansions for the normal velocity and pressure. The solution expands in the familiar form

$$\widehat{u} = F_0 + \cdots, \quad \widehat{v} = \varepsilon G_0 + \varepsilon^3 G_1 + \cdots, \quad \widehat{p} = \varepsilon^2 P_0 + \varepsilon^4 P_1 + \cdots, \tag{2.27a–c}$$

$$\alpha = \varepsilon\alpha_0 + \cdots, \quad c = \varepsilon^2 c_0 + \cdots. \tag{2.27d, e}$$

The solutions for F_0, G_0 and P_0 are as given in (2.7), with A_0 and $\widehat{P}_0$ taken to be real without loss of generality, while the correction terms G_1 and P_1 may be written in the form

$$G_1 = -\mathrm{i}\alpha_0 A_1 \frac{U_{00}}{r} + \text{purely imaginary terms}, \tag{2.28a}$$

$$P_1 = P_+^{(1)} + \alpha_0^2 A_1 I(r) + \text{purely real terms}. \tag{2.28b}$$

Here, the unknown constants A_1, $P_+^{(1)}$ are complex. Examining the behaviour of these solutions as the walls are approached, we find that (2.9), (2.10) continue to hold, and

$$\begin{aligned} \mathrm{Im}(P_1) &\to \mathrm{Im}\big(P_+^{(1)}\big) \quad \text{as } r \to 1, \\ \mathrm{Im}(P_1) &\to \mathrm{Im}\big(P_+^{(1)}\big) + \alpha_0^2 \mathrm{Im}(A_1) I(\delta) \quad \text{as } r \to \delta. \end{aligned} \tag{2.29}$$

From this latter result, we may deduce that the net jump in the imaginary part of P_1 across the core is given by

$$[\mathrm{Im}(P_1)]_-^+ = -\alpha_0^2 I(\delta)\mathrm{Im}(A_1). \tag{2.30}$$

(ii) *The inviscid shear region II+.* As mentioned above, the core region matches, above and below, to an inviscid region in which the first term in the basic flow expansion (2.3) becomes comparable with the disturbance wavespeed c: clearly this occurs at a distance of $O(\varepsilon^2)$ from each wall. In the upper region $II+$ the appropriate flow expansions are

$$U_0 = \varepsilon^2 \lambda_+^{(0)} Y_+ + \varepsilon^4 \big(\lambda_+^{(1)} Y_+ + \lambda_+^{(10)} Y_+^2\big) + \cdots, \quad r = 1 - \varepsilon^2 Y_+, \tag{2.31a, b}$$

$$\widehat{u} = u_+^{(0)} + \varepsilon^2 u_+^{(1)} + \cdots, \quad \widehat{v} = -\varepsilon^3 v_+^{(0)} - \varepsilon^5 v_+^{(1)} - \cdots, \quad \widehat{p} = \varepsilon^2 p_+^{(0)} + \varepsilon^4 p_+^{(1)} + \cdots, \tag{2.31c–e}$$

with α and c expanding as in (2.27). The resulting inviscid balances possess the simple solutions:

$$u_+^{(0)} = -A_0 \lambda_+^{(0)}, \quad v_+^{(0)} = \mathrm{i}\alpha_0 A_0 \zeta_+ - \mathrm{i}\alpha_0 \widehat{P}_0 / \lambda_+^{(0)}, \quad p_+^{(0)} \equiv \widehat{P}_0, \quad p_+^{(1)} \equiv P_+^{(1)}, \tag{2.32}$$

upon matching to the core region I. For convenience, here the solutions are expressed in terms of the variable

$$\zeta_+ = \lambda_+^{(0)} Y_+ - c_0. \tag{2.33}$$

Applying the inviscid condition of zero normal flow on $r = 1$ to the expression for $v_+^{(0)}$, we obtain

$$A_0 c_0 + \frac{\widehat{P}_0}{\lambda_+^{(0)}} = 0, \tag{2.34}$$

providing a first pressure–displacement relation. Also of importance here is the solution for the second term in the normal velocity expansion which may be written in the form

$$v_+^{(1)} = \mathrm{i}\alpha_0 A_+^{(1)} \zeta_+ + \text{imaginary terms} - \frac{\mathrm{i}\alpha_0 P_+^{(1)}}{\lambda_+^{(0)}} - \frac{\mathrm{i}\alpha_0 \widehat{P}_0}{\lambda_+^{(0)}} \left(\frac{2\lambda_+^{(10)}}{\lambda_+^{(0)2}} + \frac{1}{\lambda_+^{(0)}} \right) \zeta_+ \ln \zeta_+, \tag{2.35}$$

given here for $\zeta_+ > 0$, with the complex constant $A_+^{(1)}$ unknown. It is the final logarithmic term which demonstrates the irregular behaviour that is smoothed out by the thin linear critical layer present at $\zeta_+ = 0$. The dynamics of such a layer are well understood (Lin 1955; Stuart 1963; Reid 1965) and the only aspect of the critical-layer dynamics that concerns us here is the phase shift of $-\pi$ that arises upon crossing it. The effect of this is that the solution for $v_+^{(1)}$ when $\zeta_+ < 0$ is simply given by (2.35), but with $\ln \zeta_+$ replaced by $\ln|\zeta_+| - \mathrm{i}\pi$. From matching the real part of the first term in (2.35) as $\zeta_+ \to \infty$ with the real part of the first term in the expression (2.28a) for G_1 as $r \to 1$, we obtain

$$\mathrm{Im}\left(A_+^{(1)}\right) = \mathrm{Im}(A_1). \tag{2.36}$$

In order to determine the size of ε in terms of the Reynolds number, we need to match the behaviour in the inviscid shear region below the critical layer (i.e. for $\zeta_+ < 0$) to the flow in the viscous wall layer ($III+$) at $r = 1$. In this latter region, the basic flow is very small and the dominant balance in the governing equation (1.4b) is between $-\mathrm{i}\alpha c\widehat{u}$ and $R^{-1}q^{-2}\widehat{u}$ where q is the thickness of the layer. Since $\alpha c \sim O(\varepsilon^3)$, we see that $q \sim O(R^{-1/2}\varepsilon^{-3/2})$. The size of ε is then determined by matching the normal velocities between regions $III+$ and $II+$. The streamwise perturbation within region $III+$ must be of $O(1)$ to match with $II+$, and hence, by continuity, the normal velocity in $III+$ must be $O(\varepsilon q)$. Matching this to the term $v_+^{(1)}$ in (2.31d) we have the order of magnitude balance $\varepsilon q \sim \varepsilon^5$ and hence we deduce

$$\varepsilon = R^{-1/11}, \tag{2.37}$$

for the upper branch scaling, as for plane Poiseuille–Couette flow. The terms involving the normal velocity must balance exactly, not only in order of magnitude, and this requires more detailed analysis. Having established the scaling for ε, we now write down the expansions in the wall layer $III+$.

(iii) *Viscous wall layer* $III+$. To leading order, we have

$$\widehat{u} = \overline{u}_+, \quad \widehat{v} = -\varepsilon^5 \overline{v}_+, \quad \widehat{p} = \varepsilon^2 \widehat{p}_0, \quad r = 1 - \varepsilon^4 \overline{y}_+, \tag{2.38}$$

and substitution into the linear disturbance equations leads to a set of viscous equations with solutions

$$\overline{u}_+ = \frac{\widehat{P}_0}{c_0}(1-\exp(-m_+\overline{y}_+)), \quad \overline{v}_+ = -\frac{\mathrm{i}\alpha_0\widehat{P}_0}{c_0}\left(\overline{y}_+ + \frac{\exp(-m_+\overline{y}_+)}{m_+} - \frac{1}{m_+}\right), \qquad \widehat{p}_0 \equiv \widehat{P}_0, \quad m_+ = \left(\tfrac{1}{2}\alpha_0 c_0\right)^{1/2}(1-\mathrm{i}), \tag{2.39}$$

with the first purely imaginary term in $\overline{v}_+$ matching automatically to the corresponding term in the solution for $v_+^{(0)}$ in $II+$, in view of the pressure–displacement relation (2.34). Matching the real part of $\overline{v}_+$ as $\overline{y}_+ \to \infty$ with the real part of $v_+^{(1)}$ as $\zeta_+ \to -c_0$ (and taking into account the phase shift of $-\pi$) we obtain

$$-\frac{\widehat{P}_0}{c_0(2\alpha_0 c_0)^{1/2}} = c_0\mathrm{Im}(A_1) + \frac{\mathrm{Im}\left(P_+^{(1)}\right)}{\lambda_+^{(0)}} + \frac{\widehat{P}_0}{\lambda_+^{(0)}}\left(\frac{2\lambda_+^{(10)}}{\lambda_+^{(0)2}} + \frac{1}{\lambda_+^{(0)}}\right)(\pi c_0), \tag{2.40}$$

where we have used expression (2.36) to eliminate $A_+^{(1)}$.

(iv) *The lower layers.* In order to complete the analysis and derive the upper-branch eigenrelation, we need to consider the corresponding asymptotic regions near the inner cylinder. The details are very similar to those presented for the upper regions, the only differences being that (i) the inner cylinder's scaled velocity V_0 appears in the equations for regions $II-$ and $III-$ and (ii) because the surface of the inner cylinder is given by $r = \delta$ there are extra factors involving this parameter. The main results are as follows. First, from applying the condition of tangential flow to the solution in $II-$, the analogous result to (2.34) is

$$\frac{A_0}{\delta}(V_0 - c_0) + \frac{\widehat{P}_0 + \alpha_0^2 A_0 I(\delta)}{\lambda_-^{(0)}} = 0. \tag{2.41}$$

Eliminating A_0 between (2.34) and (2.41), we obtain a first relation between c_0 and α_0, namely,

$$c_0 = \left(\frac{V_0}{\delta} + \frac{\alpha_0^2 I(\delta)}{\lambda_-^{(0)}}\right)\left(\frac{1}{\delta} + \frac{\lambda_+^{(0)}}{\lambda_-^{(0)}}\right)^{-1}. \tag{2.42}$$

Next, from matching the normal velocity between the core I and the inviscid shear region $II-$, we obtain the result

$$\mathrm{Im}\left(A_-^{(1)}\right) = -\mathrm{Im}(A_1)/\delta, \tag{2.43}$$

where $A_-^{(1)}$ is the analogous constant to $A_+^{(1)}$ in $II-$. Finally, matching the real parts of the normal velocity between region $II-$ and the viscous wall layer $III-$ leads to the expression

$$-\frac{\widehat{P}_0\left(1-\alpha_0^2 I(\delta)/\left(c_0\lambda_+^{(0)}\right)\right)}{(c_0-V_0)(2\alpha_0(c_0-V_0))^{1/2}} = -(c_0-V_0)\frac{\mathrm{Im}(A_1)}{\delta} + \frac{\mathrm{Im}\left(P_-^{(1)}\right)}{\lambda_-^{(0)}} + \frac{\widehat{P}_0\left(1-\alpha_0^2 I(\delta)/\left(c_0\lambda_+^{(0)}\right)\right)}{\lambda_-^{(0)}}\left(\frac{2\lambda_-^{(10)}}{\lambda_-^{(0)2}} - \frac{1}{\lambda_-^{(0)}\delta}\right)\pi(c_0-V_0), \tag{2.44}$$

(cf. (2.40)), where the complex constant $P_-^{(1)}$ is the second term in the pressure expansion within region $II-$. We now have sufficient information to determine the upper-branch eigenrelation. Earlier, in (2.30), we found the net jump in pressure

across the core region I; this implies that

$$\mathrm{Im}\left(P_+^{(1)}\right) - \mathrm{Im}\left(P_-^{(1)}\right) = -\alpha_0^2 I(\delta)\mathrm{Im}(A_1). \tag{2.45}$$

We can now eliminate the unknown imaginary parts of $P_+^{(1)}$, $P_-^{(1)}$, A_1 by taking an appropriate linear combination of equations (2.40), (2.44) and using expression (2.42) for c_0 and (2.45). After some manipulation we obtain

$$\frac{\lambda_+^{(0)}}{c_0(2\alpha_0 c_0)^{1/2}} - \left(1 - \frac{\alpha_0^2 I(\delta)}{c_0\lambda_+^{(0)}}\right)\frac{\lambda_-^{(0)}}{(c_0 - V_0)(2\alpha_0(c_0 - V_0))^{1/2}} + c_0\pi\left(\frac{2\lambda_+^{(10)}}{\lambda_+^{(0)2}} + \frac{1}{\lambda_+^{(0)}}\right)$$
$$-(c_0 - V_0)\pi\left(\frac{2\lambda_-^{(10)}}{\lambda_-^{(0)2}} - \frac{1}{\lambda_-^{(0)}\delta}\right)\left(1 - \frac{\alpha_0^2 I(\delta)}{c_0\lambda_+^{(0)}}\right) = 0. \tag{2.46}$$

This is to be solved in conjunction with (2.42) and gives α_0 and c_0 as functions of V_0 and δ. Figure 8 shows the results of solving (2.42), (2.46) for α_0. Details of the method of solution are given in Appendix A. A unique solution for α_0 is found for a given V_0 and δ. Typically, α_0 increases with increasing δ (although when δ is very small there is also an increase in α_0 with decreasing δ). As V_0 is increased from zero, the value of α_0 rises slightly, falls and then increases monotonically with $\alpha_0 \to \infty$ as $V_0 \to \infty$ for all values of δ. Clearly, in this limit the upper-branch structure is breaking down, with the wavelength of the neutral mode shortening. This limit can be investigated further by examining analytically the upper-branch eigenrelations (2.42), (2.46) with V_0 asymptotically large. We find the following results:

$$\alpha_0 \sim \left(\frac{\lambda_+^{(0)}}{I(\delta)}\right)^{1/2} V_0^{1/2} + \beta_1 V_0^{-5}, \quad c_0 \sim V_0 + \beta_2 V_0^{-9/2} \quad \text{as } V_0 \to \infty, \tag{2.47a, b}$$

with the constants β_1, β_2 given by

$$\beta_1 = -\frac{\lambda_-^{(0)2}\lambda_+^{(0)}}{16\pi^2\delta^6 \ln\delta}(1-\delta^2+2\delta^2\ln\delta)^2, \quad \beta_2 = \frac{I(\delta)^{1/2}\lambda_-^{(0)2}\lambda_+^{(0)3/2}}{8\pi^2(1-\delta^2)^2\delta^4}(1-\delta^2+2\delta^2\ln\delta)^2, \tag{2.48}$$

where we have made some use of expressions (2.4), (2.5) for the skin-friction and curvature coefficients of the basic flow. These results are consistent with the numerical solution of the eigenrelation presented above. Since $c_0 \to V_0+$ as $V_0 \to \infty$, it is clear that for this upper branch mode the lower critical layer is moving towards the wall at $r = \delta$. Eventually, once V_0 has increased sufficiently, the critical layer will move inside the viscous wall layer *III*−, forming a lower-branch-type structure. While this is happening, we would expect the upper layers to be essentially unaffected, retaining their upper branch character. We therefore anticipate the formation of a 'hybrid' mode and in the next section we deduce the magnitude of V at which this new structure comes into play and we investigate the behaviour of the mode on this new scaling. We will also see that the lower-branch mode with the asymptotic behaviour identified in (2.25) also moves onto this new scaling at the same order of magnitude of V.

2.2.3. *The hybrid scaling*

As mentioned above, we expect that when V_0 is sufficiently large the lower critical layer in the upper-branch structure will move inside the viscous wall layer. Within this lower-branch-type wall layer we require the disturbance wavespeed c to be the same order of magnitude as the basic flow which takes the near-wall form

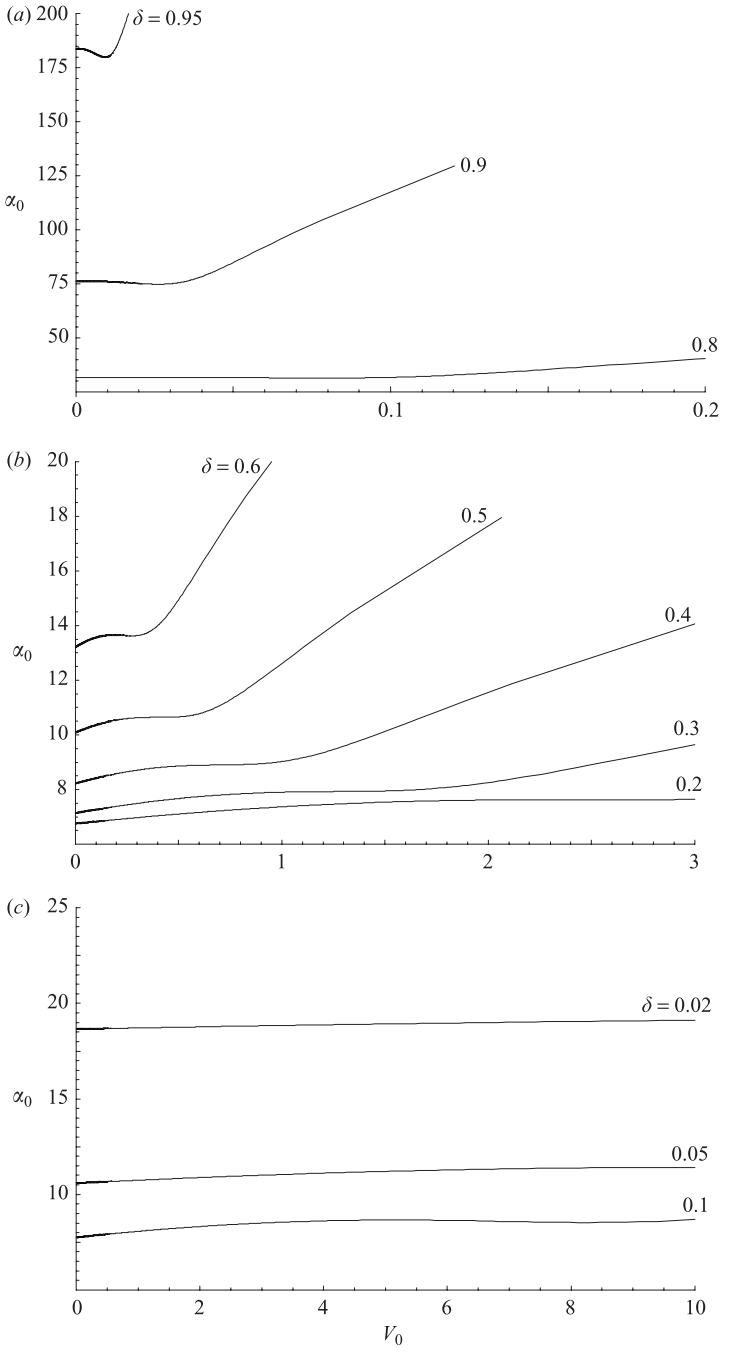

FIGURE 8. Solution of the upper branch eigenrelations (2.42), (2.46).

$\lambda_-^{(0)}(r-\delta)+R^{-2/11}V_0$. In view of this, the term (U_0-c) in (1.4*b*) becomes

$$U_0-c\sim\lambda_-^{(0)}(r-\delta)-R^{-2/11}(c_0-V_0)\sim\lambda_-^{(0)}(r-\delta)-R^{-2/11}\beta_2V_0^{-9/2},$$

upon use of the asymptotic result (2.47*b*). For the two terms to be in balance we therefore require the layer to be of thickness $y\sim(r-\delta)\sim R^{-2/11}V_0^{-9/2}$. The crucial

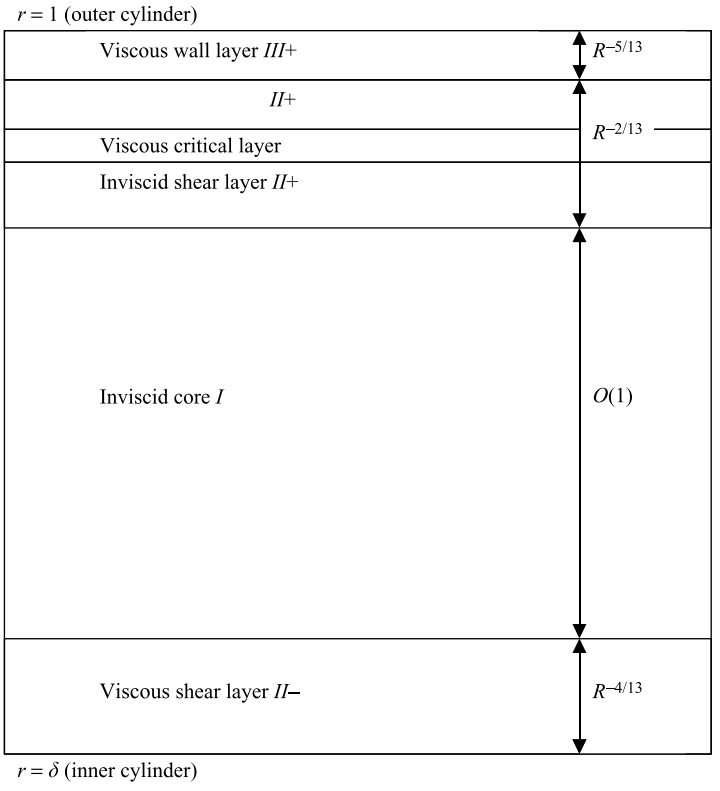

FIGURE 9. The asymptotic structure of the hybrid modes.

balance within the layer is between the term $\alpha(U_0 - c)$ and the viscous operator $R^{-1}\partial^2/\partial y^2$. Recalling the upper-branch scaling (2.27*d*), (2.37) for α and the asymptotic form (2.47*b*) we therefore have the parameter balance

$$R^{-1/11} V_0^{1/2} R^{-2/11} V_0^{-9/2} \sim R^{-1} \left(R^{-2/11} V_0^{-9/2} \right)^{-2},$$

which leads to the scalings

$$V_0 \sim R^{4/143}, \quad \alpha_0 \sim R^{2/143}, \quad c_0 \sim R^{4/143},$$

or, in terms of the original variables, a new regime in which

$$\left.\begin{aligned} V &= R^{-2/13} \overline{V}_0, \quad \alpha = R^{-1/13} \overline{\alpha}_0 + R^{-3/13} \overline{\alpha}_1 + \cdots, \\ c &= R^{-2/13} \overline{c}_0 + R^{-4/13} \overline{c}_1 + \cdots, \quad \overline{c}_0 = \overline{V}_0. \end{aligned}\right\} \tag{2.49}$$

Again, the same scalings hold in the planar case (Cowley & Smith 1985). We now analyse each of the asymptotic regions on this new scaling in turn, with the ultimate aim of determining the eigenrelation governing the behaviour of the modes with this scaling, and finding, if it exists, the cutoff velocity beyond which these modes are no longer neutral. The different regions involved are sketched in figure 9.

(i) *The core region I.* Here the scalings are exactly as on the lower and upper branches, i.e. we have

$$\widehat{u} = F_0 + \cdots, \quad \widehat{v} = \varepsilon G_0 + \varepsilon^3 G_1 + \cdots, \quad \widehat{p} = \varepsilon^2 P_0 + \varepsilon^4 P_1 + \cdots, \tag{2.50}$$

but with the small parameter ε now given by

$$\varepsilon = R^{-1/13}. \tag{2.51}$$

The same inviscid balances hold in the core as before, with the solutions and asymptotic behaviour given in (2.7), (2.28), (2.9), (2.10).

(ii) *Upper inviscid shear region II+*. This is largely unchanged from the corresponding region in the upper-branch structure with the expansions now in powers of $R^{-1/13}$. The solutions for the velocity perturbations and the pressure are precisely as given in (2.32) (with $\overline{\alpha}_0, \overline{c}_0$ replacing α_0, c_0) and the relations (2.34), (2.36) also continue to hold. There is a linear critical layer embedded in this region across which a $-\pi$ phase shift is induced, and as a result we still obtain the result

$$\mathrm{Re}\big(v_+^{(1)}\big) \to \overline{\alpha}_0\overline{c}_0\mathrm{Im}\big(A_+^{(1)}\big) + \frac{\overline{\alpha}_0\mathrm{Im}\big(P_+^{(1)}\big)}{\lambda_+^{(0)}} + \frac{\overline{\alpha}_0\widehat{P}_0}{\lambda_+^{(0)}}\left(\frac{2\lambda_+^{(10)}}{\lambda_+^{(0)2}} + \frac{1}{\lambda_+^{(0)}}\right)\overline{c}_0\pi \quad \text{as } \overline{y}_+ \to \infty. \tag{2.52}$$

(iii) *Upper wall layer III+*. The balances here remain as for the upper branch structure although the layer is now reduced in thickness to $O(R^{-5/13})$ in view of the increase in the disturbance frequency αc relative to the upper branch scaling. A consequence of the reduction in thickness is that the real part of the normal velocity here is now smaller in magnitude (by a factor ε) than the corresponding quantity in *II+*. There is therefore a mismatch in normal velocities between these layers, resulting in the expression

$$\overline{c}_0\mathrm{Im}(A_1) + \frac{\mathrm{Im}\big(P_+^{(1)}\big)}{\lambda_+^{(0)}} + \frac{\widehat{P}_0}{\lambda_+^{(0)}}\left(\frac{2\lambda_+^{(10)}}{\lambda_+^{(0)2}} + \frac{1}{\lambda_+^{(0)}}\right)\overline{c}_0\pi = 0, \tag{2.53}$$

cf. (2.40).

(iv) *Lower inviscid shear region II−*. Here the upper-branch wall layer, shear region and critical layer have merged to form a single zone in which

$$r = \delta + \varepsilon^4 Y_-, \quad \widehat{u} = u_-^{(0)} + \cdots, \quad \widehat{v} = \varepsilon^5 v_-^{(0)} + \cdots, \quad \widehat{p} = \varepsilon^2 p_-^{(0)} + \varepsilon^4 p_-^{(1)} + \cdots. \tag{2.54}$$

Substitution into the linear disturbance equations (1.4) reveals that

$$p_-^{(0)} \equiv 0, \tag{2.55}$$

and therefore from the core solution (2.10) and the pressure–displacement relation (2.34), we deduce that

$$\widehat{P}_0 = -\overline{\alpha}_0^2 A_0 I(\delta) = -\lambda_+^{(0)} A_0 \overline{c}_0, \tag{2.56}$$

thus fixing the leading-order neutral wavenumber in terms of the scaled inner cylinder velocity as

$$\overline{\alpha}_0 = \left(\frac{\lambda_+^{(0)}}{I(\delta)}\right)^{1/2} \overline{V}_0^{1/2}, \tag{2.57}$$

(since $\overline{c}_0 = \overline{V}_0$), which of course matches back to the upper-branch regime via the asymptote (2.47*a*). In order to determine the eigenrelation for the hybrid scaling, we need to investigate the leading-order balances within this layer. They are

$$\left.\begin{aligned} &\mathrm{i}\overline{\alpha}_0 u_-^{(0)} + v_-^{(0)\prime} = 0, \\ &\mathrm{i}\overline{\alpha}_0\big(\lambda_-^{(0)}Y_- - \overline{c}_1\big)u_-^{(0)} + \lambda_-^{(0)}v_-^{(0)} = -\mathrm{i}\overline{\alpha}_0 p_-^{(1)} + u_-^{(0)\prime\prime}, \quad p_-^{(1)\prime} = 0, \end{aligned}\right\} \tag{2.58}$$

with

$$u_-^{(0)} = v_-^{(0)} = 0 \text{ on } Y_- = 0, \quad u_-^{(0)} \to A_0\lambda_-^{(0)}/\delta \quad \text{as } Y_- \to \infty. \tag{2.59}$$

In addition, from the core result (2.30) we have

$$\mathrm{Im}\big(p_-^{(1)}\big) = \mathrm{Im}\big(p_+^{(1)}\big) + \overline{\alpha}_0^2 \mathrm{Im}(A_1) I(\delta). \tag{2.60}$$

Equations (2.58) with boundary conditions (2.59) constitute a standard 'lower-deck' problem which can easily be solved as in the lower-branch case to yield

$$-\overline{\alpha}_0^2 p_-^{(1)} = \big(\mathrm{i}\overline{\alpha}_0\lambda_-^{(0)}\big)^{5/3} \frac{\mathrm{Ai}'(\overline{\xi}_-)}{\kappa(\overline{\xi}_-)} \frac{A_0}{\delta}, \tag{2.61}$$

$$\overline{\xi}_- = -\frac{\mathrm{i}^{1/3}\overline{\alpha}_0\overline{c}_1}{\big(\overline{\alpha}_0\lambda_-^{(0)}\big)^{2/3}} \equiv -\mathrm{i}^{1/3}\overline{s}_-, \tag{2.62}$$

with notation as in § 2.2.1. Taking the imaginary part of this expression and using (2.60), (2.53) and (2.56), we finally obtain the hybrid eigenrelation

$$\overline{V}_0^{13/6} = -\left(\frac{\lambda_+^{(0)}}{I(\delta)}\right)^{-1/6} \frac{\big(\lambda_-^{(0)}\big)^{5/3}}{\pi\delta} \left(\frac{2\lambda_+^{(10)}}{\lambda_+^{(0)}} + 1\right)^{-1} \mathrm{Im}(g(\overline{s}_-)), \tag{2.63}$$

with $g(s)$ given in (2.17). For given $\overline{V}_0$, the leading-order neutral wavenumber $\overline{\alpha}_0$ can be calculated from (2.57), with (2.63) giving the corresponding value(s) for the wavespeed correction $\overline{c}_1$. Figure 10 shows $\overline{c}_1$ plotted versus $\overline{V}_0$ for various values of δ from the numerical solution of (2.63). It can be seen that for a given δ and for $\overline{V}_0$ up to a critical value ($\overline{V}_c$, say), there are typically two solutions, although there is a small range of $\overline{V}_0$ where there are four modes. For $\overline{V}_0 > \overline{V}_c$, there are no solutions on this scaling and thus $\overline{V}_c$ represents a scaled cutoff velocity for modes of this type. The origins of the two typical modes on this scaling can be traced back to the upper and lower branch structures by analysing the limit $\overline{V}_0 \to 0$. In this limit, (2.63) implies that $\mathrm{Im}(g(\overline{s}_-)) \to 0$, leading to two possibilities: (i) $\overline{s}_- \to s_0$ or (ii) $\overline{s}_- \to \infty$. If (i) holds then we have from (2.62) and (2.23):

$$\overline{c}_1 \sim \left(\frac{\lambda_+^{(0)}}{I(\delta)}\right)^{-1/6} \big(\lambda_-^{(0)}\big)^{2/3} s_0 \overline{V}_0^{-1/6} \quad \text{as } \overline{V}_0 \to 0. \tag{2.64}$$

From comparison with the asymptotic expression (2.26), we can see that this mode is in fact the continuation of the lower-branch solution which shortened its wavelength on that scaling as V was increased. On the other hand, if (ii) holds we can use the asymptotic form (2.22) for $g(s)$, in which case the eigenrelation (2.63) reduces, after some manipulation, to:

$$\overline{c}_1 \sim \beta_2 \overline{V}_0^{-9/2} \quad \text{as } \overline{V}_0 \to 0, \tag{2.65}$$

with β_2 given in (2.48). It can be seen therefore by comparison with (2.47*b*) that this mode is the continuation of the upper-branch mode on the new scaling. These two modes form the upper and lower branches of a single neutral curve on the hybrid scaling, as can be seen in figure 10.

2.3. *Summary of the asymptotic results*

We have analysed the linear neutral stability of circular Couette–Poiseuille flow at asymptotically large Reynolds number and investigated the behaviour of the neutral modes as the inner cylinder velocity is increased. The main findings are as follows.

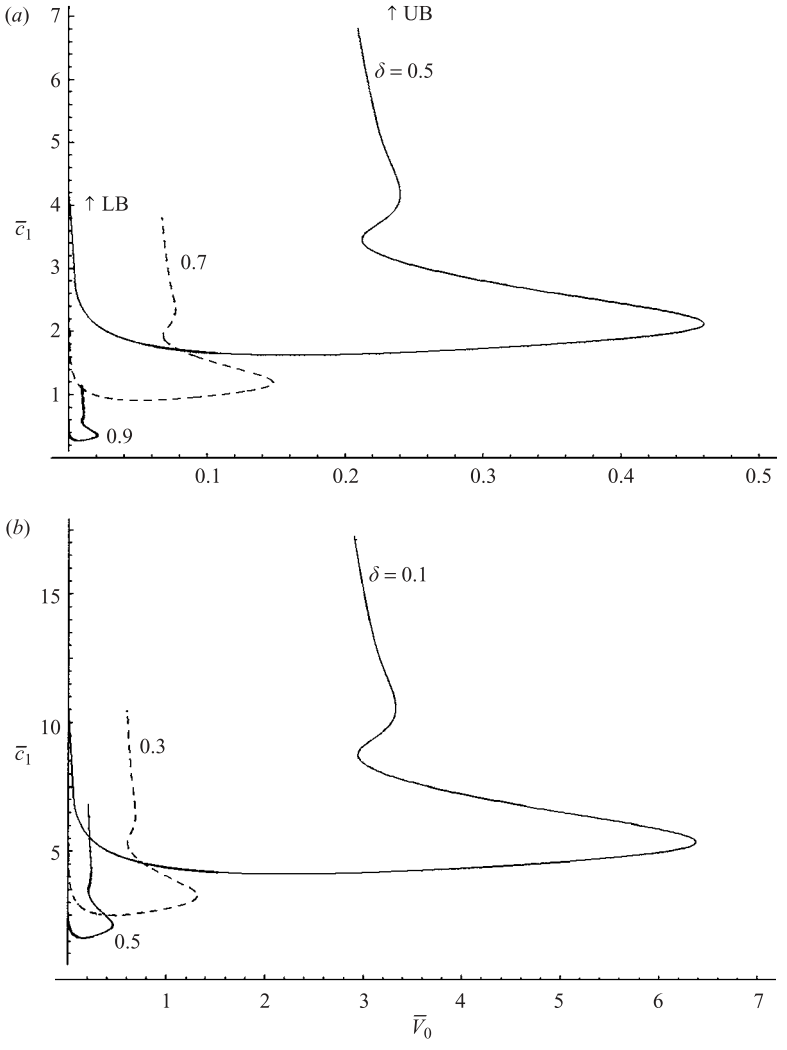

FIGURE 10. Solution of the eigenrelation (2.63) for the hybrid scaling. The arrows in (*a*) indicate how the two branches of each neutral curve match back to the upper branch (UB) and lower branch (LB) scalings.

First, we showed in § 2.1 that the flow is inviscidly stable and therefore any instability must be viscous in nature. We then moved on to discuss viscous instabilities in § 2.2.

When the inner cylinder is moving sufficiently slowly, there are instability modes described by a lower-branch scaling (§ 2.2.1). The number of modes varies with radius ratio δ and inner cylinder velocity V. When $V = 0$, there is a single solution for all values of δ. When $0.92 \leqslant \delta < 1$, two extra pairs of solutions are created as V is increased on this scaling. One of these solutions eventually 'breaks out' of this scaling when V increases to $O(R^{-2/13})$ and moves onto the hybrid scaling (§ 2.2.3) where it forms the lower branch of a single neutral curve. This mode then vanishes on the new scaling at the cutoff velocity $R^{-2/13}\overline{V}_c$. The other four solutions continue to be described by the original lower-branch scaling until $V \sim O(1)$. Their subsequent evolution will be described in the next section. When $0.47 < \delta < 0.92$, the same events

occur as above but now only one extra pair of solutions are generated on the lower-branch scaling, and when $\delta < 0.47$, no extra solutions are generated at all.

A separate mode evolves on the upper-branch scaling (§2.2.2) which holds until $V \sim O(R^{-2/13})$. No extra solutions are generated as V is increased and the mode eventually 'breaks out' of this scaling, forming the upper branch of a single neutral curve on the hybrid scaling. The mode survives on this new scaling until the cutoff velocity $R^{-2/13}\overline{V}_c$ is reached where the $O(1)$ quantity $\overline{V}_c$ increases with decreasing δ.

In order to complete our description of the behaviour of the neutral modes at high Reynolds number, it is necessary to consider the fate of the lower-branch solutions that do not experience a cutoff on that scaling. Depending on the value of δ there can be either one or two pairs of such modes, or no such modes if $\delta \lesssim 0.47$.

2.4. *The ultimate fate of the lower-branch modes*

These modes, which form on the lower-branch scaling, have wavenumbers of $O(R^{-1})$ when V is increased to $O(1)$, according to the asymptotic behaviour (2.21) and the scaling (2.11). In order to follow their further evolution as V is increased on this new scaling we need to derive a new governing equation. This is achieved by taking the limit $R \to \infty$ of the circular Orr–Sommerfeld equation (1.6) but with αR remaining $O(1)$, (implying that $\alpha \to 0$). Thus, the modes are governed by

$$(U_0 - c)(\phi'' - \phi'/r) - (U_0'' - U_0'/r)\phi = (\mathrm{i}\alpha R)^{-1}(\phi^{\mathrm{iv}} - 2\phi'''/r + 3\phi''/r^2 - 3\phi'/r^3), \quad (2.66)$$

with

$$\phi = \phi' = 0 \quad \text{on } r = \delta,\ r = 1. \quad (2.67)$$

The neutral curves for given αR, V and δ are computed using the same method (a continuation approach using Chebyshev collocation and Newton's method) to be described in §3 when we solve the full circular Orr–Sommerfeld equation. Figure 11 shows a first set of what may be termed 'cutoff curves', as beyond a certain value of V there is no instability on this lengthscale. It can be seen that the cutoff velocity V_c increases as δ decreases until $\delta \simeq 0.5$. Below this value of δ, the cutoff curves become closed, shrinking to a point at about $\delta \simeq 0.428$, a phenomenon also reported by Gittler (1993). The significance of the curves being closed will be explained when we move on to solve the circular Orr–Sommerfeld equation at finite values of R in §3. The vanishing of the modes at this value of δ is consistent with the earlier finding that no lower-branch modes exist when $\delta \lesssim 0.52$, apart from the one that moves on to the hybrid scaling and therefore experiences cutoff before V becomes $O(1)$.

As in the case of planar Poiseuille–Couette flow (Cowley & Smith 1985), there is a second set of cutoff curves for a range of values of δ – these represent the continuation of the second set of modes created on the lower branch scaling. The curves are shown in figure 12 on a logarithmic scale. The cutoff velocities involved are much smaller than for the first pair of modes and the typical values of αR are much larger, typically of order 10^9, suggesting that these modes may only exist at very large Reynolds number. We will indeed see that this is the case when we carry out our finite-Reynolds-number computations.

Based on all our asymptotic analysis, we present schematic diagrams of the regions of instability at large Reynolds number in figure 13. Of course, this picture does not tell the whole story: for example, we have no information about the critical values of R for each unstable region, and there may be neutral curves that close up at finite R that would not be found by this asymptotic approach. To obtain the full picture we need to complement our asymptotic findings with computations at finite Reynolds number.

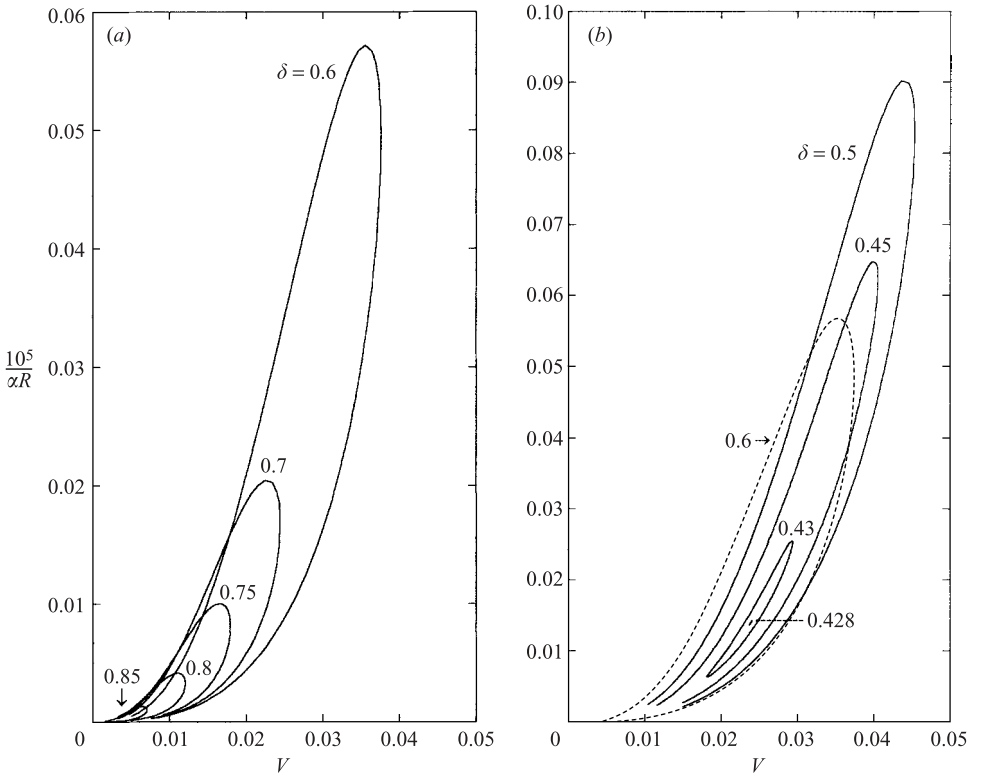

FIGURE 11. The first set of neutral stability 'cutoff' curves from the numerical solution of (2.66) for various values of δ.

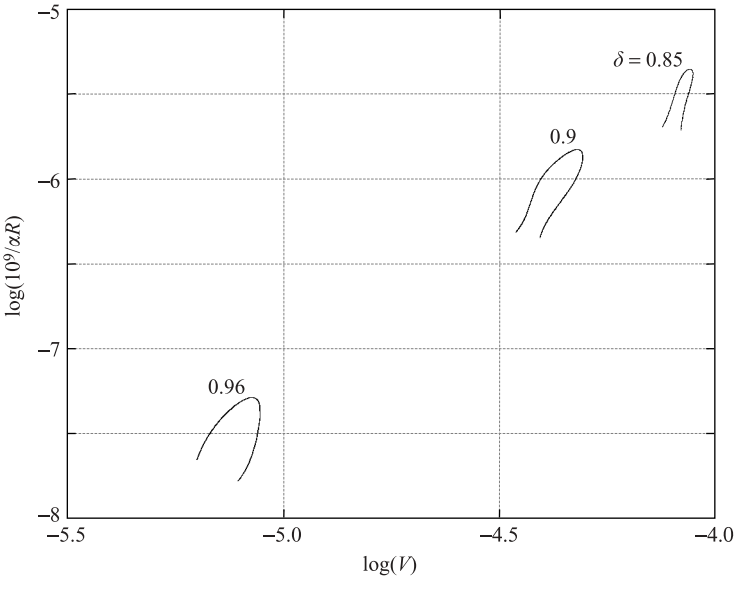

FIGURE 12. The second set of 'cutoff' curves from the numerical solution of (2.66) for various values of δ.

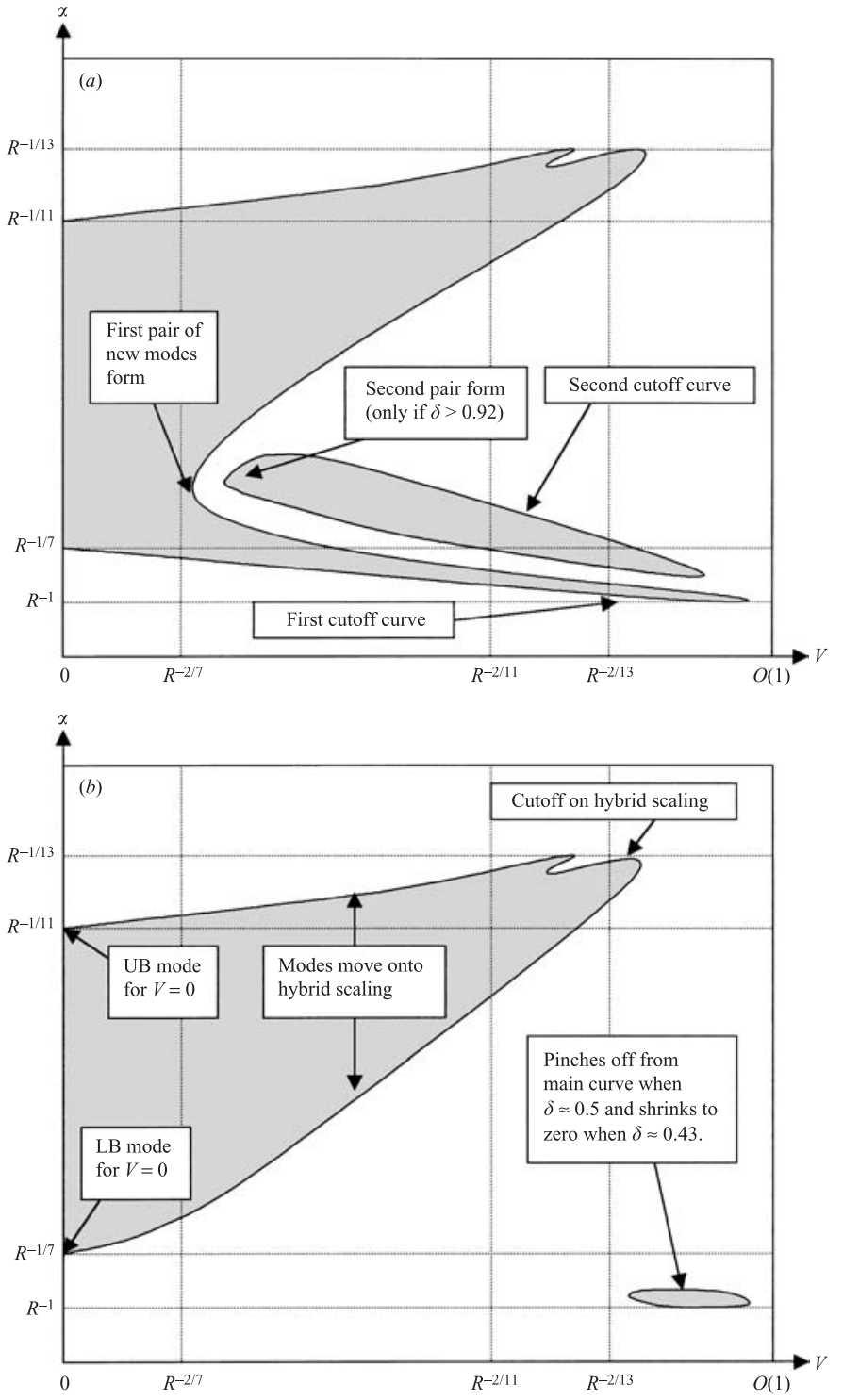

FIGURE 13. Sketches of the stability diagram at high Reynolds number, based on the asymptotic analysis of § 2. The shaded regions are unstable.

3. Finite-Reynolds-number numerical solutions

In this section, we solve the circular Orr–Sommerfeld equation numerically, guided by our asymptotic results, but mindful that they only provide a partial picture of the stability properties of this flow. We describe the numerical method used here first and then describe the numerical results and how they fit in with our earlier asymptotic findings.

3.1. *Numerical method*

In order to solve (1.6) and determine neutral curves for given values of inner cylinder velocity V, radius ratio δ and Reynolds number, we apply a collocation method using Chebyshev polynomials; this appears now to be the standard approach for solving this type of eigenvalue problem owing to its simplicity, speed and accuracy. The reader is referred to Gottlieb, Hussaini & Orszag (1984) for a full discussion of the theory and to Khorrami, Malik & Ash (1989) or Schmid & Henningson (2001) for the main details. The idea is that the function ϕ is expanded in a series of Chebyshev polynomials T_n as

$$\phi = \sum_{n=1}^{M+1} a_n T_{n-1}(\xi), \quad r = \tfrac{1}{2}((1+\delta) - (1-\delta)\xi),$$

where ξ is evaluated at the Gauss points $\xi_j = \cos(\pi(j-1)/M)$, $j = 1, \ldots, M+1$. The expression for ϕ is substituted into (1.6), and evaluated at the interior points $j = 3, \ldots, M-1$. The boundary conditions are also written in Chebyshev form, giving us a total of $M+1$ equations which can be expressed in matrix form as

$$\boldsymbol{B}\boldsymbol{a} = \lambda \boldsymbol{C}\boldsymbol{a} \quad \text{where } \boldsymbol{a} = (a_1, a_2, \ldots, a_{M+1})^T, \quad \lambda = -\mathrm{i}\Omega, \quad \Omega = \alpha c, \tag{3.1}$$

with $\boldsymbol{B}, \boldsymbol{C}$ square matrices of dimension $M+1$, containing derivatives of the Chebyshev polynomials, and also dependent on $\alpha^2, \alpha R$ and the basic flow parameters δ and V. The boundary conditions are chosen to occupy the first two and last two rows of the matrix $\boldsymbol{B}$. The generalized eigenvalues λ from this problem can be found using a package such as MatLab, and spurious solutions corresponding to the boundary conditions can easily be identified and eliminated. The number of collocation points used was sufficient to obtain six decimal places of accuracy in the computed values of λ, and typically $M = 240$ proved sufficient, although this was increased for large values of R.

Since we wish to map out neutral curves in the (R, α)-plane, however, solving the eigenvalue problem (3.1) at each (R, α) point is extremely time-consuming as all but one of the eigenvalues is discarded at each level in an iterative process. It is much more efficient to determine one point on the neutral curve in this fashion and then use a continuation technique in which we find the next point on the neutral curve directly by solving a *nonlinear* problem using Newton's method. The procedure is outlined below.

First, we split the eigenvector, and the matrices $\boldsymbol{B}$ and $\boldsymbol{C}$, into their real and imaginary parts by writing

$$\boldsymbol{a} = \boldsymbol{x} + \mathrm{i}\boldsymbol{y}, \quad \boldsymbol{B} = \boldsymbol{B}_r + \mathrm{i}\boldsymbol{B}_i, \quad \boldsymbol{C} = \boldsymbol{C}_r + \mathrm{i}\boldsymbol{C}_i.$$

The matrix problem, for a given δ and V, can now be written as two real equations:

$$\boldsymbol{B}_r(\alpha, R)\boldsymbol{x} - \boldsymbol{B}_i(\alpha, R)\boldsymbol{y} = \Omega(\boldsymbol{C}_r(\alpha, R)\boldsymbol{y} + \boldsymbol{C}_i(\alpha, R)\boldsymbol{x}), \tag{3.2a}$$

$$\boldsymbol{B}_i(\alpha, R)\boldsymbol{x} + \boldsymbol{B}_r(\alpha, R)\boldsymbol{y} = -\Omega(\boldsymbol{C}_r(\alpha, R)\boldsymbol{x} - \boldsymbol{C}_i(\alpha, R)\boldsymbol{y}), \tag{3.2b}$$

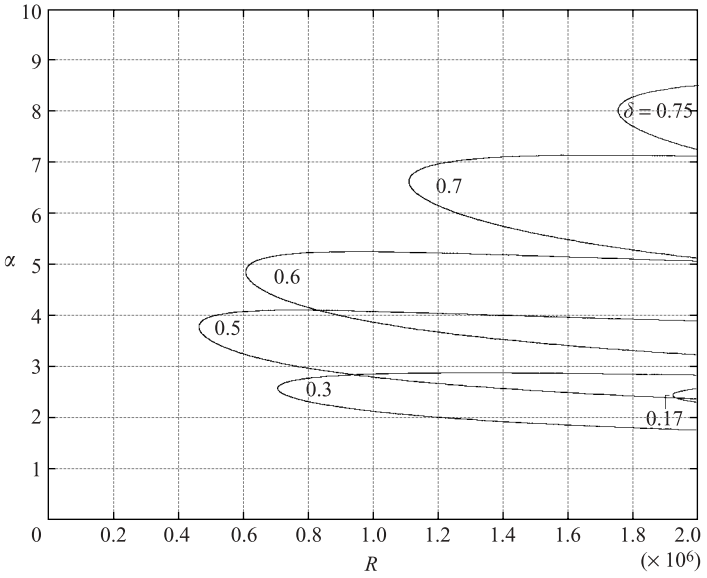

FIGURE 14. Neutral stability curves from the numerical solution of (1.6) for the case $V = 0$ and various values of δ.

where Ω is real for neutral modes. In addition, we are free to impose two conditions on the eigenvector $\boldsymbol{a}$. It is convenient to choose

$$\boldsymbol{x}^T\boldsymbol{x} + \boldsymbol{y}^T\boldsymbol{y} = 1, \quad \boldsymbol{x}^T\boldsymbol{y} = 0. \tag{3.3a, b}$$

Finally, we wish to compute the solution at a small distance ($\widehat{\varepsilon}$ say) away from the previous point (R_0, α_0) say, on the neutral curve. Thus we impose, for given $\widehat{\varepsilon}$:

$$(\alpha - \alpha_0)^2 + (R - R_0)^2 - \widehat{\varepsilon}^2 = 0. \tag{3.4}$$

This gives us a total of $2M + 5$ equations (3.2a, b), (3.3a, b), (3.4) for the $2M + 5$ unknowns $\boldsymbol{x}, \boldsymbol{y}, \alpha, \Omega, R$. Provided we have a good initial guess (supplied by the solution at the previous point on the neutral curve), these nonlinear equations can be solved efficiently using Newton's method, since the Jacobian matrix can be calculated explicitly. Typically, $\widehat{\varepsilon}$ was taken in the range $0.001 < \widehat{\varepsilon} < 1$, depending upon our precise location on the curve and the values of the other parameters. The method can easily be modified to generate curves of any given growth rate.

The cutoff problem of § 2.4 was solved in the same way except that in that case only δ is fixed, with V allowed to vary and the matrices depend on the quantities αR and V.

3.2. *Numerical results*

We start by presenting in figure 14 neutral curves in the (R, α)-plane for the case when the inner cylinder is at rest. In this situation, the asymptotic analysis and numerical results by previous workers predict a unique curve for each value of δ. We show curves for a range of values of δ and it is evident that the critical Reynolds number R_{crit} falls as δ is decreased in the range $0.5 \lesssim \delta < 1$ and then rises rapidly with further decrease in δ. Simultaneously, the typical wavelength of instability increases and the band of unstable wavelengths decreases. At first sight, the behaviour of the critical Reynolds number seems in contradiction with earlier results (Mott & Joseph 1968; Sadeghi & Higgins 1991) where a monotonic decrease in Reynolds number was reported as δ was

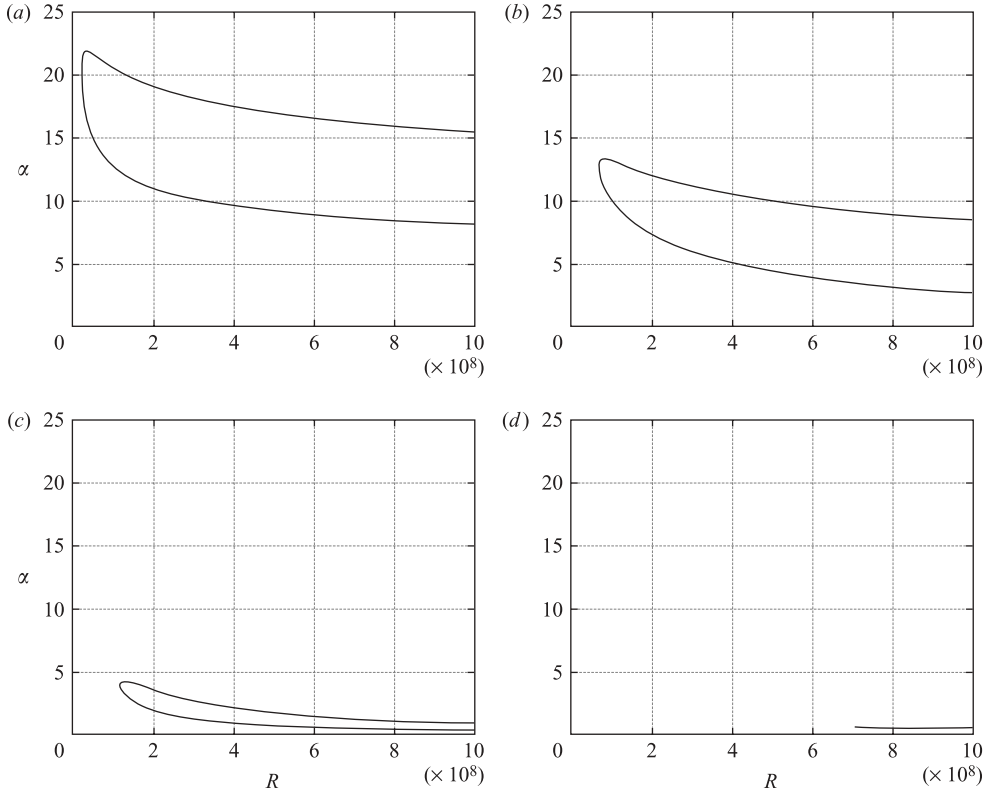

FIGURE 15. Neutral stability curves with $\delta = 0.9$ for the following values of V: (*a*) 0; (*b*) 0.001; (*c*) 0.003; (*d*) 0.00327.

decreased. The discrepancy, however, is purely due to the difference in definition of R: we base our Reynolds number on outer cylinder radius and pressure gradient (as this is appropriate for the thread injection application) while in the aforementioned references the gap width and maximum velocity were used. The difference between the definitions is most noticeable when δ is near unity and the curves are in perfect agreement with previous work when allowance is made for this.

In figure 15, we concentrate on the case $\delta = 0.9$ and investigate what happens to the neutral curve as V increases. Our asymptotic analysis (see the sketch in figure 13) has suggested that the following features should emerge from our computations: (i) we should observe a splitting of the neutral curve at a certain value of V; (ii) at a slightly larger value of V another curve should form; (iii) of these three curves we expect one to close up at finite Reynolds number at a critical value of V, (this is the curve that forms on the hybrid scaling, § 2.2.3) and the other two should retreat to $R = \infty$ at $O(1)$ values of V (these are the cutoff curves in § 2.4). From the sequence of figure 15(*a*)–15(*d*) we observe only a single neutral curve retreating to infinity. In order to uncover the rest of the features anticipated above, we need to examine smaller non-zero values of V at higher values of R. The higher values of R are achieved within the current numerical scheme by employing a rescaling of the problem, and this is described in Appendix B. The results are presented in figure 16 (with δ remaining equal to 0.9). At very small V, a pocket of stability, forming at $R = \infty$, penetrates the neutral curve, and advances to the left on the stability diagram, effectively slicing the neutral curve

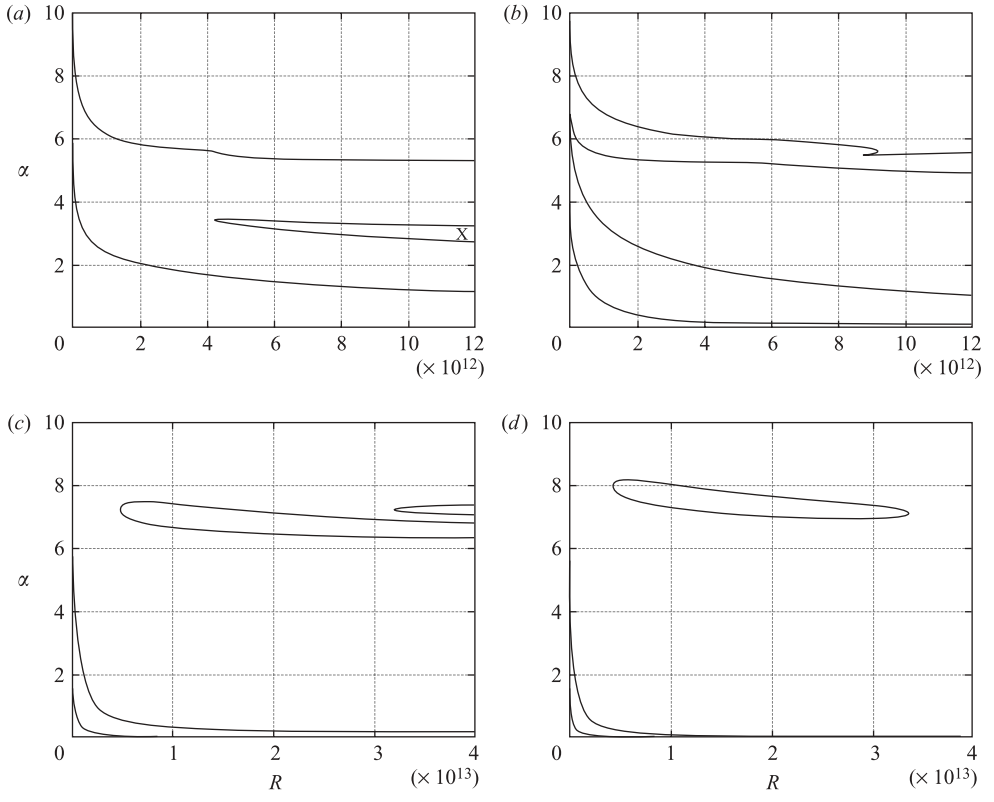

FIGURE 16. Neutral stability curves with $\delta = 0.9$ for the following values of V: (*a*) 0.44×10^{-4}; (*b*) 1.3×10^{-4}; (*c*) 2.5×10^{-4}; (*d*) 3.2×10^{-4}.

in two. Simultaneously, a kink develops on the upper stability boundary; this is the same phenomenon observed in the solution of the hybrid eigenrelation (figure 10). We now see that there are multiple regions of instability: for example, in figure 16(*b*) at $R = 9 \times 10^{12}$ there are three separate regions of disturbance growth. As V is increased further, the top curve splits into two, with one part moving to larger Reynolds number while the other closes up. Simultaneously, the lower curve moves to longer wavelengths. The top curve on figure 16(*d*) arises on the hybrid scaling while the lower curve represents two of the modes that persist on the lower branch scaling. Beyond a value of $V \simeq 0.004$, only the lower curve persists and it is this curve which is captured in figure 15. Thus far, we have seen evidence of the hybrid modes and one pair of lower-branch modes. There should be a second pair of lower-branch modes: these do exist, but numerically only at extremely large values of R. Figure 17 shows this second 'lower-branch' neutral curve: it forms within the stable intrusion (marked with an 'X' on figure 16*a*) which itself forms within the original neutral curve. This second curve only exists for a small range of values of V and retreats to $R = \infty$ in accordance with the results of § 2.4. Although this second curve may be present at other values of δ, we will not discuss it further as it seems to be of very little physical significance.

We have seen from our results for $\delta = 0.9$ that the stability diagram is quite complicated for non-zero V, with neutral curves existing simultaneously on the hybrid and lower branch scalings, but only at very large values of R and very small

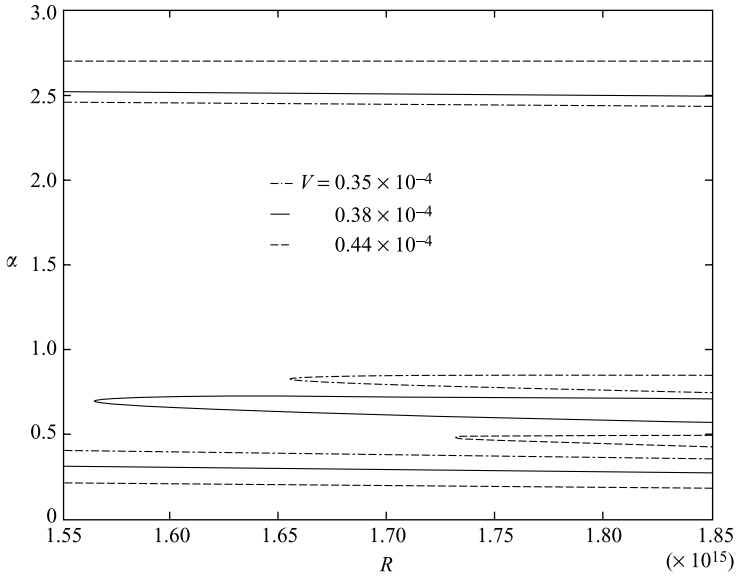

FIGURE 17. Neutral stability curves with $\delta = 0.9$ at large values of the Reynolds number, from the numerical solution of (1.6) under the rescaling of Appendix B. Dot-dashed curves: $V = 0.35 \times 10^{-4}$; solid curves: $V = 0.38 \times 10^{-4}$; dashed curves: $V = 0.44 \times 10^{-4}$. The flow is unstable inside the 'finger-like' curves and outside the outer curves.

values of V. As δ is decreased, however, this complicated behaviour spreads to smaller Reynolds numbers and exists over a larger range of values of V. To demonstrate this, we present neutral curves for the case $\delta = 0.55$. Figure 18 shows the corresponding neutral stability diagrams and how they alter as V is increased. A familiar pattern is emerging: first, we have a unique curve for $V = 0$; then, at small non-zero V, a stable intrusion spreads from right to left, eventually penetrating almost to the nose of the curve and slicing it into two almost equal-sized smaller curves (figure 18*d*). The top curve is the 'hybrid curve' and the bottom one is the 'lower-branch curve'. As V is increased further to 0.0125 (figure 18*e*), we see that the hybrid curve has thinned substantially and is now closed; slightly beyond this value of V it disappears completely leaving the lower-branch scaling governing the stability properties of the flow. This curve then retreats to infinity at finite V as predicted in § 2.4, leaving the flow linearly stable at all Reynolds numbers for all V beyond this critical value. Although Sadeghi & Higgins report only single neutral curves at given δ and V there is definite evidence in their figure 5 ($\delta = 0.5$) that they are actually following two separate curves in their numerical computations.

For values of δ in the range $0.45 \lesssim \delta < 1$, the behaviour of the neutral curves as V is increased is as described above. Some modifications occur, however, when δ is decreased further. This is connected with our observation that in the 'cutoff' results of § 2.4 the cutoff curve in the $(V, \alpha R)$-plane becomes closed at $\delta \simeq 0.43$. Suppose that the range of V over which there is instability is $V_1 \leqslant V \leqslant V_2$. This means that the lower branch curve must actually be closed at finite Reynolds number for $V < V_1$; it then 'attaches to infinity' at $V = V_1$, and retreats to $R = \infty$ in the normal way as $V \to V_2-$. We can witness these events occurring numerically in the sequence of figure 19(*a*)–19(*g*) for $\delta = 0.43$. The difference to the previous results at larger δ is that the incision is formed towards the lower branch of the neutral curve, and as a

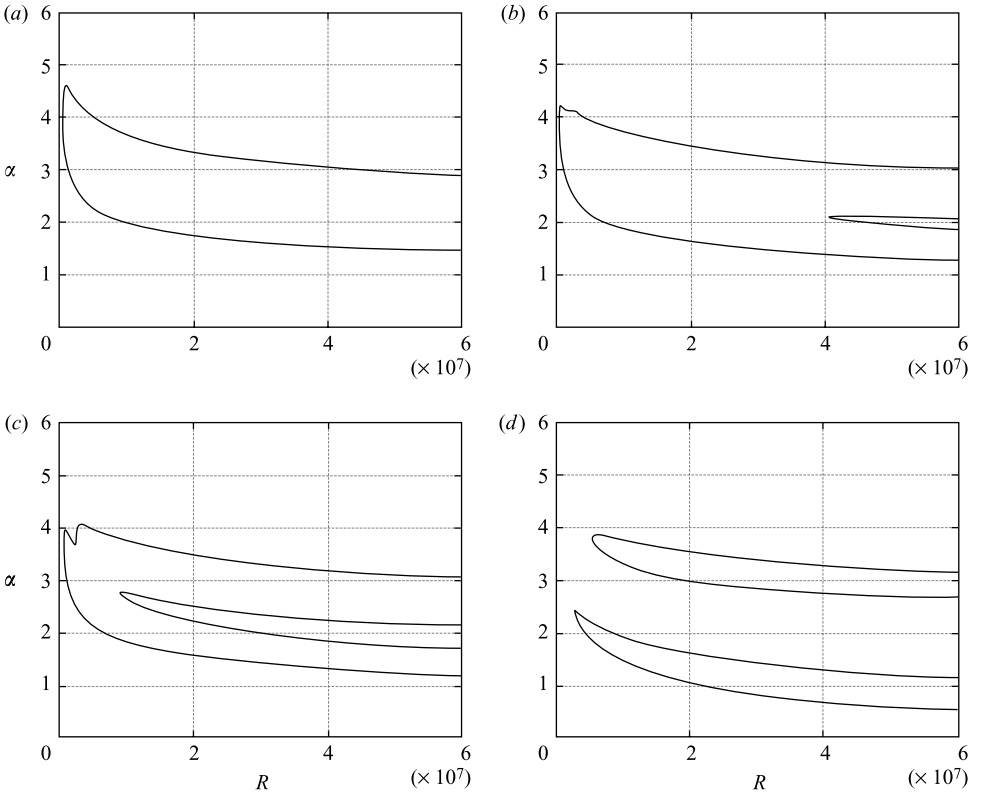

FIGURE 18(*a–d*). For caption see facing page.

result a closed curve is 'sliced off' (figure 19*d*). At this stage, it is the upper hybrid curve which dominates, in contrast to the situation at larger δ. We see that when V has increased to 0.02, the lower curve has apparently become attached to infinity and is retreating rapidly in that direction, leaving the hybrid scaling to govern the stability properties. This curve eventually disappears at finite Reynolds number when $V \simeq 0.03$, leaving a linearly stable flow at all Reynolds numbers.

Below $\delta \simeq 0.42$, the analysis of § 2.4 predicts no cutoff curves and so we would expect our finite-Reynolds-number calculations to yield a single hybrid-scaled curve at given V. This is indeed the case: for $\delta = 0.4$, we show in figure 20, a series of neutral curves for increasing V. There is now no intrusion forming and therefore no curve-splitting occurs. The upper- and lower-branch scalings for $V = 0$ simply unite on the hybrid scaling (as indicated schematically in figure 13) to form a unique neutral curve that eventually closes up at finite Reynolds number and disappears when $V \simeq 0.035$. It can be seen that the disappearing point is fairly close to the nose of the $V = 0$ curve; there is no retreat to larger values of R in this case. For values of δ less than 0.4, the sequence of events as V increases remains the same as shown in figure 20.

The case shown in figure 18(*d*) when $\delta = 0.55$, $V = 0.01$ is particularly interesting. Here we have two distinct neutral curves of similar widths and with similar critical Reynolds numbers. It is found, however, that the manner in which growing modes inside each of these curves extract energy from the basic flow is rather different. This can be demonstrated by computing the product of the Reynolds stress and the basic velocity gradient and examining its radial distribution for each mode. If we write the

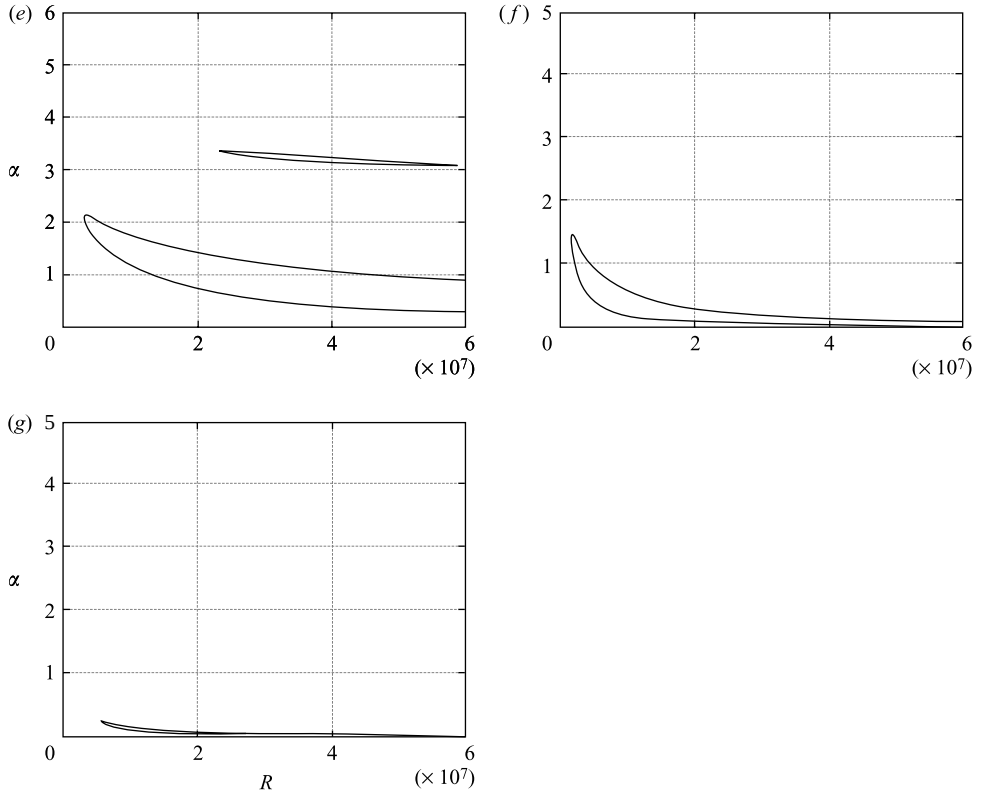

FIGURE 18. Neutral stability curves with $\delta = 0.55$ for the following values of V: (*a*) 0; (*b*) 0.004; (*c*) 0.005; (*d*) 0.01; (*e*) 0.0125; (*f*) 0.03; (*g*) 0.0425.

energy equation in the standard form

$$\frac{\mathrm{d}I_1}{\mathrm{d}t} = I_2 + R^{-1} I_3,$$

Drazin (2002), then the term of interest here is I_2, which in our notation is given by

$$I_2 = \frac{\pi}{\alpha^2} \exp(2\alpha c_i t) \int_\delta^1 E(r)\,\mathrm{d}r, \quad E(r) = \frac{U_0'(r)}{r} \mathrm{Im}(\phi^* \phi'(r)).$$

When $E > 0$, energy is extracted from the basic flow by the disturbance, whereas if $E < 0$, energy is transferred back to the basic flow. To illustrate the different distributions we choose the fastest growing modes inside the two neutral curves for $\delta = 0.55$, $V = 0.01$ at $R = 10^7$. These have the following properties:

$$\alpha_1 \simeq 1.73, \quad c_{01} \simeq 0.013 + 9.6 \times 10^{-5}\mathrm{i}, \quad \alpha_1 c_{01i} \simeq 1.66 \times 10^{-4},$$
$$\alpha_2 \simeq 3.55, \quad c_{02} \simeq 0.020 + 9.2 \times 10^{-5}\mathrm{i}, \quad \alpha_2 c_{02i} \simeq 3.25 \times 10^{-4}.$$

The subscript 1 refers to a growing mode within the lower curve (a 'lower-branch' mode). It is evident that in this case the 'hybrid mode' within the upper curve (subscript 2) has the larger growth rate of the two. In figure 21, we plot E versus r for each of these modes. It can be seen that for the lower-branch mode, $E < 0$ near the moving wall and energy is lost by the disturbance. The energy flow is in the opposite direction near the outer wall of the annulus and the profile is fairly symmetric

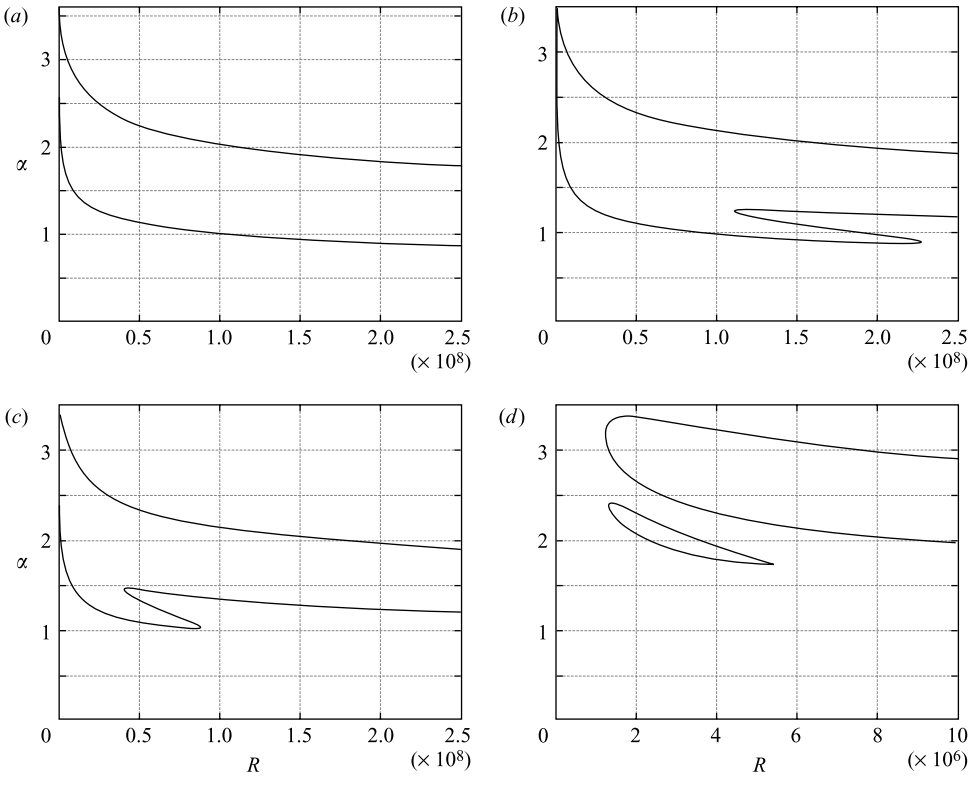

FIGURE 19(*a–d*). For caption see facing page.

about the centre of the gap. The hybrid mode, by contrast, gains most of its energy near the inner cylinder and also extracts a small amount of energy from the basic flow near the outer wall. This latter energy distribution seems to be typical of modes for which the real part of the wavespeed exceeds significantly the value of the inner wall velocity V, while the E-profile of the lower branch mode is common to modes for which the real part of $V-c$ is positive or close to zero. These observations are consistent with the findings of Sadeghi & Higgins (1991).

Our finite-Reynolds-number results may be summarized as follows.

(i) For $V=0$, there is a unique neutral curve for all values of δ with the critical Reynolds number smallest for $\delta \simeq 0.5$.

(ii) The effect of increasing V is to increase R_{crit} from its $V=0$ value. At sufficiently large V (for all values of δ), the flow is linearly stable at all R.

(iii) As V is increased for δ in the range $0.425 \lesssim \delta < 1$, the neutral curve splits into two curves. Growing modes inside the top curve extract most of their energy from the basic flow near the inner cylinder, while modes inside the lower curve gain their energy near the outer cylinder. The lower curve, governed by the lower-branch scaling, retreats to $R=\infty$ at finite V, while the upper curve (on the hybrid scaling) closes up at finite R, eventually disappearing at a critical value of V which may be more or less than the value of V at which the lower curve disappears. Broadly speaking, when $0.45 \lesssim \delta < 1$ and V is $O(1)$, the lower curve is the more important (e.g. possesses larger growth rates, applies over a larger range of wavelengths, has a lower value of R_{crit}), while for $\delta < 0.45$ the upper curve dominates.

(iv) For $\delta \lesssim 0.42$, only the upper hybrid curve exists.

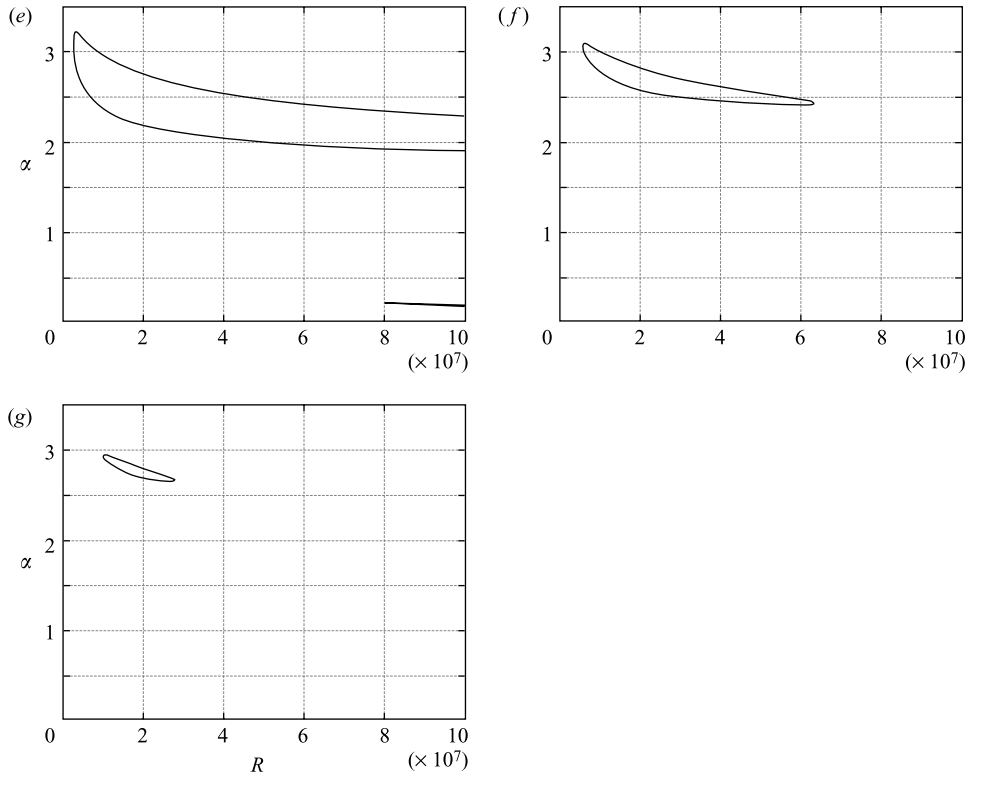

FIGURE 19. Neutral stability curves with $\delta = 0.43$ for the following values of V: (*a*) 0; (*b*) 0.004; (*c*) 0.005; (*d*) 0.008; (*e*) 0.02; (*f*) 0.027; (*g*) 0.0285.

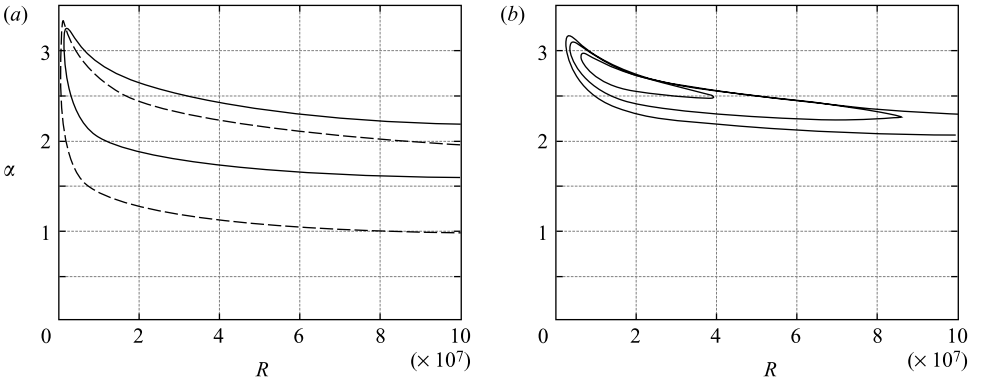

FIGURE 20. Neutral stability curves with $\delta = 0.4$ for: (*a*) $V = 0$ (dashed), $V = 0.015$ (solid); (*b*) outer to inner: $V = 0.028, 0.031, 0.034$.

(v) In addition, for sufficiently large δ, there is also another neutral curve on the lower-branch scaling which forms inside the intrusion into the original curve. This curve only exists over a small range of V, however, and at extremely large Reynolds number: therefore, we expect it to be of very little practical importance.

The asymptotic and numerical results presented here have focused on the case of $V > 0$. In Appendix C, we show how the analysis must be altered when $V < 0$. Although there are modifications to the asymptotic analysis, the overall conclusion is

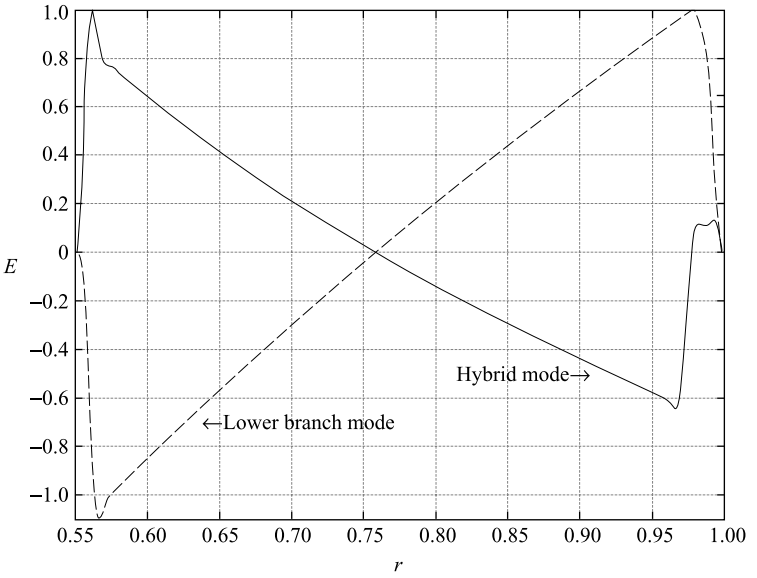

FIGURE 21. The radial distribution $E(r)$ of the energy supply for the fastest growing modes with $\delta = 0.55$, $V = 0.01$ and $R = 10^7$.

the same as for $V > 0$, namely, that over a large range of δ there are, for a given V, two neutral curves with the properties discussed above, although in the $V < 0$ case, the hybrid curve appears to be much less significant.

In the final section, we discuss the relevance of these results to the medical application of thread injection and we show how the linear neutral modes found here connect to their nonlinear counterparts as the amplitude of the perturbation is increased.

4. Discussion

4.1. *Nonlinear stability and the application to thread injection*

The basic circular Poiseuille–Couette flow studied in this paper is relevant to the thread injection of medical implants. In this newly devised surgical technique, a thread of porous material (representing the inner cylinder) is injected within a fluid held in a cylindrical container. For more details of this process, the reader is referred to Frei *et al.* (2000). The typical Reynolds number at which instability was reported in their experiments was about 3×10^4 using the non-dimensionalization adopted in the present paper, while the corresponding R_{crit} predicted by the linear analysis is about 4×10^5. There is therefore an order of magnitude disagreement between theory and experiment, suggesting that nonlinear effects play an enhanced role in the transition process for this flow, presumably in a similar way to that for the flow through a single pipe.

In Walton (2003), with the medical application in mind, the nonlinear stability of this basic flow was studied asymptotically at large values of the Reynolds number and amplitude-dependent nonlinear neutral modes were found for an $O(1)$ range of values of V and δ with $V > c$. The values of V for which nonlinear modes exist are much larger than the linear cutoff velocities found here, while the structure of the modes is similar to that for the hybrid scaling (where $V < c$) except that the upper critical layer is now nonlinear and has moved out into the core region.

A natural question to ask is how the present linear neutral curves connect to the nonlinear modes as the disturbance amplitude is increased. In fact, the latter structure can be found to be a natural nonlinear continuation of the linear regime by reconsidering the hybrid eigenrelation (2.63) for an enhanced disturbance size. It is well known (Benney & Bergeron 1969; Haberman 1972) that as the perturbation amplitude increases, the phase shift ϕ across the critical layer decreases in magnitude (essentially the 'π' in the denominator of (2.63) is replaced by ϕ). It is then clear from (2.63) that the effect of reducing ϕ is to decrease the values of the wavespeed correction $\overline{c}_1$ on the two branches of the neutral curve in figure 10, i.e. for weakly nonlinear perturbations, the mode wavespeed approaches the inner cylinder velocity V from below. As $\phi \to 0$, a balance is re-established between the normal velocity perturbations within the inviscid shear layer $II+$ and the viscous wall layer $III+$. By examining the expressions (2.39) and (2.52), we see that an order of magnitude balance is possible provided that

$$\varepsilon^6 \frac{\overline{\alpha}_0 \widehat{P}_0}{\overline{c}_0(\overline{\alpha}_0\overline{c}_0)^{1/2}} \sim \varepsilon^5 \overline{\alpha}_0 \widehat{P}_0 \overline{c}_0 \phi, \tag{4.1}$$

with $\varepsilon = R^{-1/13}$. For the linear critical layer, ϕ is $O(1)$ and therefore the terms above differ in magnitude by a factor ε, as discussed in § 2.2.3. On the hybrid scaling we have

$$\overline{c}_0 \sim \overline{V}_0, \quad \overline{\alpha}_0 \sim \overline{V}_0^{1/2}, \tag{4.2}$$

so that (4.1) can be rewritten as

$$\varepsilon \sim \overline{V}_0^{11/4} \phi. \tag{4.3}$$

The dynamics of the weakly nonlinear critical layer are discussed in Appendix D where it is established that

$$\phi \sim \overline{\alpha}_0{}^{-1} \overline{c}_0^{-3/2} \overline{\Delta}^{-3/2} \quad \text{as } \overline{\Delta} \to \infty, \tag{4.4}$$

for disturbances of amplitude $\Delta = \varepsilon^6 \overline{\Delta}$. Writing (4.4) in terms of $\overline{V}_0$ and substituting into (4.3) we obtain the amplitude–velocity balance

$$\overline{\Delta} \sim \varepsilon^{-2/3} \overline{V}_0^{1/2}.$$

The strongly nonlinear neutral mode structure referred to earlier applies for $O(1)$ cylinder velocities V, i.e. $\overline{V}_0 \sim O(\varepsilon^{-2})$. In this setting, the appropriate disturbance amplitude is therefore

$$\Delta = \varepsilon^6 \overline{\Delta} \sim \varepsilon^{16/3} \overline{V}_0^{1/2} \sim R^{-1/3}.$$

This is precisely the amplitude of the nonlinear neutral modes studied in Walton (2003), and they possess $O(1)$ wavenumbers and wavespeeds in view of the scalings (4.2), (2.49), with a phase shift across the critical layer $\phi \sim O(R^{-1/2})$, from (4.4). Thus, as the amplitude of the disturbance is increased, the upper and lower branches of the hybrid neutral curve (figure 10) 'lift-up' from the zero-amplitude plane and the curve extends to $O(1)$ values of V, where there is now a nonlinear cutoff velocity on this new scaling. It is evident from this that the effect of nonlinearity is to increase the range of instability of the basic circular Poiseuille–Couette flow and it would appear to be these nonlinear effects, through their enhanced correction to the mean flow, that hold the key to explaining the experimentally observed instabilities in this flow.

Of course, in practice, there are many other effects that must be taken into account when attempting to describe the instability of thread–annular flow and our results

should be regarded as merely a first step in describing the phenomenon. In reality, the thread will possess some flexibility and its position within the outer cylinder may not always be concentric: both these factors could affect the instability process considerably. Other important issues are whether the thread is sufficiently long for the basic flow to have become fully developed in space and whether the injection process occurs over a long enough time interval for full temporal evolution of the flow to be achieved. Finally, the importance of non-symmetric disturbances needs to be addressed more fully, an area we now discuss in a little more detail.

4.2. *Non-symmetric disturbances*

Although this paper has concentrated on the axisymmetric linear stability of Poiseuille–Couette flow, the stability to asymmetric disturbances of the form $\exp(\mathrm{i}\alpha(x-ct)+\mathrm{i}N\theta)$ with N an integer, is also of theoretical and practical interest, as remarked above. Numerical calculations were carried out by Sadeghi & Higgins (1991), and, appropriately rescaled, are consistent with results obtained by the present author. The main conclusions are as follows. For a given δ, the effect of increasing V is stabilizing (as in the axisymmetric case) and there is a cutoff velocity which once again can be calculated from the stability equations in the limit $R\to\infty, \alpha R\to O(1)$. The $N=1$ mode is found to possess a slightly lower critical Reynolds number than the corresponding axisymmetric disturbance, while higher modes are progressively more stable and possess smaller cutoff velocities. As in the $N=0$ case, the effect of decreasing δ is to at first make the flow more unstable by lowering the critical Reynolds number. For $N=1$, the flow is least stable when $\delta\simeq 0.2$, with further decrease in δ leading to a rapid increase in R_{crit}. For higher values of N, the critical Reynolds number is larger, with the most unstable radius ratio tending towards unity as N is increased.

In contrast to the axisymmetric case, there is no numerical evidence for the existence of multiple neutral curves. The added complexity of the governing equations for $N\neq 0$ makes it difficult to perform the type of asymptotic analysis that proved so successful in predicting multiple neutral curves for the $N=0$ case. If there is more than one curve at given V and δ, it seems likely that the curve splitting occurs at very small V and at high Reynolds number, rendering the secondary curve of little practical importance in the non-symmetric case.

The author wishes to express his thanks to Dr G. Moore for suggesting the continuation approach outlined in § 3.1 and the comments of the referees are acknowledged gratefully.

Appendix A. The solution of the upper-branch eigenrelation

In § 2.2.2, we showed that the upper-branch scaling leads to modes governed by equations (2.42) and (2.46). To demonstrate that there is only one mode on this scaling (for a given δ and V_0), it is convenient to define the parameter

$$\mu = 1 - V_0/c_0 \quad (>0). \tag{A 1}$$

Equation (2.42) can then be rewritten as

$$\alpha_0^2 = \frac{c_0}{I(\delta)}\left(\lambda_+^{(0)} + \frac{\lambda_-^{(0)}\mu}{\delta}\right), \tag{A 2}$$

while, after some manipulation, (2.46) can be recast in the form

$$c_0^{11/4} = C_1(\mu)/C_2(\mu), \tag{A 3}$$

where

$$C_1(\mu) = \frac{(I(\delta))^{1/4}}{2^{1/2}} \left(\lambda_+^{(0)} + \frac{\lambda_-^{(0)}\mu}{\delta}\right)^{-1/4} \left(\lambda_+^{(0)} + \frac{\left(\lambda_-^{(0)}\right)^2 \mu^{-1/2}}{\delta\lambda_+^{(0)}}\right),$$

$$C_2(\mu) = \frac{2(1-\delta^2)\pi}{|\ln\delta|} \left(\frac{1}{\left(\lambda_+^{(0)}\right)^2} + \frac{\mu^2}{\delta^3\lambda_+^{(0)}\lambda_-^{(0)}}\right).$$

Thus, for a given δ and μ, the unique value of c_0 can be found from (A 3), with α_0 then following from (A 2). Finally, the corresponding value of V_0 can be obtained from (A 1). This procedure is repeated for various values of δ, leading to the results presented in figure 8.

Appendix B. The numerical solution of the cylindrical Orr–Sommerfeld equation in the small-gap limit

In order to elicit the fine detail of the neutral curve for values of δ close to unity, it proves necessary to compute solutions to the cylindrical Orr–Sommerfeld equation (1.6) at very large values of the Reynolds number and at very small non-zero values of the inner cylinder velocity V. In this Appendix, we show how, by a suitable rescaling of the problem, this can be achieved accurately. At the same time, this rescaling allows us to compare our results in the limit $\delta \to 1$ with those of Cowley & Smith (1985) for planar Poiseuille–Couette flow where the basic flow is given by

$$U_{CS} = \tfrac{3}{2}(1-\xi^2) + (1+\xi)V_{CS}, \quad (-1 \leqslant \xi \leqslant 1).$$

In order to achieve these aims, we first define $2\pi Q_0$ to be the undisturbed flux through the annulus when $V = 0$, i.e.

$$Q_0 = \int_\delta^1 r\left(1 - r^2 + (\delta^2 - 1)\frac{\ln r}{\ln\delta}\right) \mathrm{d}r.$$

Next, consider the linear stability of the basic flow

$$\widehat{U}_0 = \frac{(1+\widehat{V})}{Q_0} U_0\left(r, \frac{3Q_0V}{2}, \delta\right),$$

where $U_0(r, V, \delta)$ is the basic flow given in (1.2), and $\widehat{V}$ is related to V by

$$V = \frac{4\widehat{V}}{3(1-\delta)(1+\widehat{V})}.$$

Suppose that the associated linear neutral wave for a given V and δ has wavenumber $\widehat{\alpha}$ at Reynolds number $\widehat{R}$. It is clear that this corresponds to an instability of the original profile (1.2), with inner cylinder velocity $3Q_0V/2$, in which the neutral wavenumber is unchanged, but the Reynolds number is given by

$$\frac{(1+\widehat{V})\widehat{R}}{Q_0}.$$

This quantity will be considerably larger than $\widehat{R}$, since Q_0 will be small when δ is close to unity. In addition, the corresponding cylinder velocity will be much smaller than V for the same reason. Thus, by solving the $\widehat{U}_0$-instability problem, we can obtain the solution to the U_0-problem at the desired large Reynolds numbers and small cylinder velocities.

In order to compare our results with the planar case in the limit $\delta \to 1$, we consider the solution of the $\widehat{U}_0$-instability problem, and perform the rescaling

$$\overline{U}_0 = (1-\delta)\widehat{U}_0, \quad \overline{\alpha} = \tfrac{1}{2}(1-\delta)\widehat{\alpha}, \quad \overline{R} = \tfrac{1}{2}\widehat{R}, \quad \overline{c} = (1-\delta)\widehat{c}.$$

We can then show that

$$\overline{U}_0 \to U_{CS} \text{ as } \delta \to 1, \quad \text{with } V_{CS} \equiv \widehat{V}.$$

Additionally, in this limit, the circular Orr–Sommerfeld equation (1.6) reduces to its planar counterpart:

$$(\overline{U}_0 - \overline{c})(\phi'' - \overline{\alpha}^2\phi) - \overline{U}_0''\phi = (\mathrm{i}\overline{\alpha}\overline{R})^{-1}(\phi^{iv} - 2\overline{\alpha}^2\phi'' + \overline{\alpha}^4\phi),$$

with a prime denoting differentiation with respect to ξ. Thus, $\overline{\alpha}$ and $\overline{R}$ are the wavenumber and Reynolds number of the corresponding two-dimensional disturbance of plane Poiseuille–Couette flow. We were able to reproduce Cowley & Smith's results in this limit and this rescaling of the problem was particularly useful for finding the second set of 'cutoff curves' shown in figure 12.

Appendix C. Solutions for negative inner cylinder velocities

Although of less relevance to the thread-injection problem, we discuss here for completeness the solution of the axisymmetric linear stability problem when $V < 0$. (Equivalently this can be regarded as the situation when the inner cylinder is at rest and the outer cylinder has positive velocity).

For this case, since the neutral wavespeed lies between the minimum and maximum flow velocities, we must allow for the possibility that $c_0 < 0$, and this brings out some new features in the asymptotic analysis. We discuss briefly in turn how the solutions of the lower, upper and hybrid eigenrelations are altered from those described in the main text (where $V > 0$), and then we present some results at finite Reynolds number.

(i) *Lower branch.* The scalings are exactly as derived in § 2.2.1, leading to the eigenrelation (2.19), but in view of the fact that c_0 could be negative, with $c_0 - V_0$ remaining positive, we need to examine the range $-\infty < s_+ < \infty$, $s_- \geqslant 0$. Numerical analysis of (2.19) shows that, for small negative V_0, there is a unique solution and, for a range of δ near unity, this is supplemented by a further two solutions that are created at finite negative V_0. As $V_0 \to -\infty$, all three solutions persist, with s_+ and s_- remaining finite. As in the case $V > 0$, these solutions acquire long-wave characteristics, with $\alpha \sim O(R^{-1})$, and exist up to $O(1)$ negative values of V, forming the upper and lower branches of one neutral curve and the lower branch of a second curve. The latter curve is much more significant, in practice, as it exists over a wider range of values of δ and turns out to possess a much smaller critical Reynolds number. The origin of the upper branch of this second curve will be found subsequently (recall that for $V > 0$ there were four solutions of this type, providing the upper and lower branches of both curves).

In addition to these 'finite-s' modes, there are two other modes that need to be discussed. The first of these has $s_- \to \infty$, $s_+ \to s_0$ as $V_0 \to -\infty$ and represents the

situation where the lower critical layer moves away from the inner cylinder surface. This is the exact opposite situation to that described in the main text, and the asymptotic behaviour, analogous to (2.25), (2.26) is found to be

$$V_0 \sim -\left(\frac{\delta I(\delta)}{\lambda_-^{(0)}}\right)\alpha_0^2, \quad c_0 \sim \left(\frac{\lambda_-^{(0)}}{\delta I(\delta)}\right)^{-1/6} \left(\lambda_+^{(0)}\right)^{2/3} s_0(-V_0)^{-1/6}, \quad \text{as } V_0 \to -\infty.$$

This matches to the hybrid mode scaling, forming the lower branch of a neutral curve, in exactly the same way as indicated in the main text for $V > 0$.

Finally, we have a mode for which $s_+ \to -\infty$, $s_- \to \infty$ as $V_0 \to -\infty$. No analogous mode exists for $V > 0$, but a similar solution was found by Cowley & Smith (1985) for plane Poiseuille–Couette flow. However, the curvature effects here lead to a quite different asymptotic behaviour from that outlined in their paper. Analysis of (2.19) in this limit shows that

$$V_0 \propto -\alpha_0^2, \quad c_0 \sim \left(1 + \left(\frac{\lambda_-^{(0)}}{\lambda_+^{(0)}}\right)^4 \frac{1}{\delta^2}\right)^{-1} V_0, \quad \text{as } V_0 \to -\infty.$$

The resulting shorter-wavelength mode moves on to the upper-branch scaling to be discussed next.

(ii) *Upper branch.* The scales are precisely as in § 2.2.2, but now two modes are possible, corresponding to the continuation of the $V = 0$ upper-branch mode for which μ in Appendix A is positive, and the continuation of the final lower-branch mode discussed above, where $\mu < 0$. For the first of these modes, the asymptotic behaviour is found to be

$$\alpha_0 \propto (-V_0)^{1/2}, \quad c_0 \propto (-V_0)^{-9/2}, \quad \text{as } V_0 \to -\infty,$$

cf. (2.47), and this can be shown to match to the hybrid scaling where it forms the upper branch of a neutral curve to be discussed shortly.

The second mode exists over a finite negative range of μ. Since $c_0 < 0$ for this mode, the upper branch analysis of § 2.2.2 needs to be modified slightly (in particular, the expression for m_+ in (2.39) is adjusted appropriately). The modified eigenrelation can be solved in a similar way to that discussed in Appendix A, and numerical solutions and asymptotic analysis show that as V_0 is decreased through negative values, the wavenumber at first rises, reaches a maximum and then tends to zero, according to

$$\alpha_0 \propto (-V_0)^{-5} \quad \text{as } V_0 \to -\infty.$$

Thus, when V_0 increases to $O(R^{2/11})$, i.e. V becomes $O(1)$, the wavenumber α has decreased to $O(R^{-1})$ and has evolved into a long wave, forming the upper branch of the second neutral curve, discussed in (i), that exists at $O(1)$ negative values of V.

(iii) *Hybrid modes.* The scales are as discussed in § 2.2.3 and allow us to describe the situation where the lower layer becomes of upper-branch type while the upper layer retains a lower-branch character. As remarked earlier, this is the exact opposite scenario to the $V > 0$ case and is caused by the fact that when V is decreased through negative values, the maximum flow velocity moves ever closer to the upper wall. The analysis proceeds in a similar way to that outlined in the main text and leads us to the eigenrelation

$$(-\overline{V}_0)^{13/6} = -\left(\frac{\lambda_-^{(0)}}{\delta I(\delta)}\right)^{-1/6} \frac{\left(\lambda_+^{(0)}\right)^{5/3}\delta}{\pi} \left(\frac{2\lambda_-^{(10)}}{\lambda_-^{(0)}} - \frac{1}{\delta}\right)^{-1} \mathrm{Im}(g(\overline{s}_+)),$$

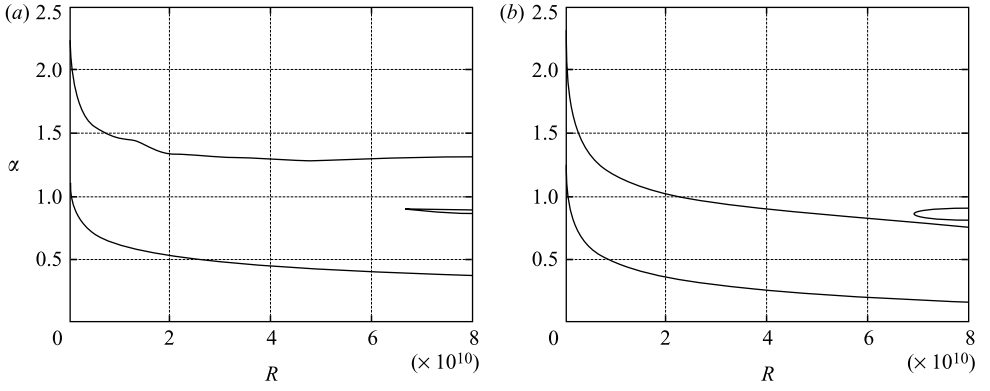

FIGURE 22. Neutral stability curves with $\delta = 0.55$ for (*a*) $V = -0.001$; (*b*) $V = -0.002$.

cf. (2.63). Numerical solutions of this relation indicate, for each value of δ, the existence of a cutoff velocity on the hybrid scaling. In general, the magnitudes of the cutoff velocities are rather smaller than their $V > 0$ counterparts.

(iv) *Solution at finite Reynolds number*. On the basis of the asymptotic analysis just presented, we expect that finite-Reynolds-number calculations will generally produce two neutral curves in the (R, α)-plane: the upper one representing the hybrid mode scaling and the lower one characteristic of a long-wave disturbance evolving from the lower branch scaling. As an example, we show in figure 22 the results of a numerical calculation for $\delta = 0.55$ and various negative values of V. If we compare with the results for $V > 0$ (figure 18), we see that (i) the stable intrusion is formed as before, but when $V = -0.001$ (figure 22*a*), it is only present at very high Reynolds number ($R > 6 \times 10^{10}$) and extends over only a very narrow band of wavenumbers; (ii) as $-V$ is increased, a second neutral curve is formed (figure 22*b*) with the formation occurring at a much smaller magnitude of inner cylinder velocity and with a much larger critical Reynolds number than for the $V > 0$ case; (iii) further increase in $-V$ leads to the retreat of this second curve. On the basis of these observations, it appears that the second curve plays only a minor role in the stability properties of the flow. As a consequence, the cutoff velocity at any value of δ can be calculated from the 'reduced' Orr–Sommerfeld problem described in § 2.4. These cutoff velocities have been calculated previously by Gittler (1993) and the main feature is that they are larger in magnitude than their $V > 0$ counterparts. In addition, cutoff velocities exist for all values of δ, i.e. there is no analogue of the closed-curve behaviour shown in figure 11(*b*) for $V > 0$.

The imposition of a negative inner cylinder velocity therefore has the effect of making the flow more unstable relative to a positive cylinder velocity of the same magnitude. The stationary configuration, however, is always the most unstable for a given radius ratio.

Appendix D. The weakly nonlinear critical layer on the hybrid scaling

Here, we investigate the effect on the critical layer in the hybrid region (where $\varepsilon = R^{-1/13}$) of increasing the disturbance size. The balance in this layer is between viscous effects and the inertial operator $(U_0 - c)\partial/\partial x$, with $\partial/\partial x \sim O(\varepsilon)$. If the variable ζ_+ $(= \lambda_+^{(0)} Y_+ - \overline{c}_0)$ is of order q say, then $(U_0 - c) \sim O(\varepsilon^2 q)$ and we have the inertial-viscous balance $\varepsilon^3 q \sim R^{-1}(\varepsilon^2 q)^{-2}$, leading to the critical-layer thickness $q \sim \varepsilon^2$ (relative to the shear layer $II+$).

Having established the thickness of the critical layer, we can begin to formulate the velocity and pressure expansions within it. First, we note that the basic flow assumes the form

$$U_0 = \varepsilon^2 \overline{c}_0 + \varepsilon^4 \lambda_+^{(0)} \widetilde{y} + \cdots + \varepsilon^8 \lambda_+^{(10)} \widetilde{y}^2 + \cdots. \tag{D 1}$$

Here, $\widetilde{y}$ is the $O(1)$ variable within the critical layer (with $r = 1 - \varepsilon^2 \overline{c}_0 / \lambda_+^{(0)} - \varepsilon^4 \widetilde{y}$). In the linear critical layer, the streamwise perturbation expansion is

$$\Delta \widehat{u} = -\Delta A_0 \lambda_+^{(0)} + \Delta \varepsilon^2 u_{cl} + \cdots, \tag{D 2}$$

while for the normal velocity we have

$$\Delta \widehat{v} = -\Delta \varepsilon^3 \mathrm{i} \overline{\alpha}_0 \overline{c}_0 A_0 - \Delta \varepsilon^5 \mathrm{i} \overline{\alpha}_0 A_0 \lambda_+^{(0)} \widetilde{y} - \Delta \varepsilon^7 v_{cl} + \cdots,$$

using the solutions established in (2.32*a*, *b*), (2.34). Weakly nonlinear effects come into play when $\Delta \sim \varepsilon^6 \overline{\Delta}$, with $\overline{\Delta}$ of $O(1)$, for then the second term in the perturbation expansion (D2) becomes comparable with the quadratic term in the basic flow expansion (D1). Then, from substitution into the Navier–Stokes equations (1.1), the critical-layer problem can be posed in the streamfunction form

$$\overline{\alpha}_0 \lambda_+^{(0)} \widetilde{y} \frac{\partial^3 \psi}{\partial \widetilde{\xi} \partial \widetilde{y}^2} - \overline{\Delta} \overline{\alpha}_0 \overline{c}_0 A_0 \sin \widetilde{\xi} \frac{\partial^3 \psi}{\partial \widetilde{y}^3} = \frac{\partial^4 \psi}{\partial \widetilde{y}^4}, \tag{D 3}$$

where $u_{cl} = \partial \psi / \partial \widetilde{y}$, $v_{cl} = -\overline{\alpha}_0 \partial \psi / \partial \widetilde{\xi}$ and $\widetilde{\xi} = \overline{\alpha}_0 (x - \overline{c}_0 t)$. The appropriate matching conditions to the surrounding shear region can be shown to be

$$\frac{\partial \psi}{\partial \widetilde{y}} \sim \lambda_+^{(10)} \widetilde{y}^2 + \overline{\Delta}^{1/2} \widehat{\lambda}^+ \widetilde{y} - \overline{\Delta} A_0 \lambda_+^{(0)} \overline{c}_0 \left(\frac{2\lambda_+^{(10)}}{\lambda_+^{(0)2}} + \frac{1}{\lambda_+^{(0)}} \right) (\ln \widetilde{y})(\cos \widetilde{\xi}) \quad \text{as } \widetilde{y} \to +\infty,$$

$$\frac{\partial \psi}{\partial \widetilde{y}} \sim \lambda_+^{(10)} \widetilde{y}^2 + \overline{\Delta}^{1/2} \widehat{\lambda}^- \widetilde{y} - \overline{\Delta} A_0 \lambda_+^{(0)} \overline{c}_0 \left(\frac{2\lambda_+^{(10)}}{\lambda_+^{(0)2}} + \frac{1}{\lambda_+^{(0)}} \right) (\ln |\widetilde{y}| \cos \widetilde{\xi} - J(\widetilde{\xi})) \quad \text{as } \widetilde{y} \to -\infty,$$

with the phase shift ϕ given by

$$\phi = \frac{1}{\pi} \int_0^{2\pi} J(\widetilde{\xi}) \sin \widetilde{\xi} \, \mathrm{d}\widetilde{\xi}.$$

Here, the quantity $\widehat{\lambda}^+ - \widehat{\lambda}^-$ represents the unknown jump in vorticity across the critical layer. This can be related to the phase shift by integrating (D3) with respect to $\widetilde{\xi}$ and $\widetilde{y}$ and applying the matching conditions. This leaves

$$\phi = \frac{2}{\overline{\alpha}_0 A_0^2 \overline{c}_0^2 \lambda_+^{(0)}} \left(\frac{2\lambda_+^{(10)}}{\lambda_+^{(0)2}} + \frac{1}{\lambda_+^{(0)}} \right)^{-1} (\widehat{\lambda}^+ - \widehat{\lambda}^-) \overline{\Delta}^{-3/2}.$$

In general, the determination of the vorticity jump, and hence the phase shift, is a numerical problem. Our interest here, however, lies in the limit $\overline{\Delta} \to \infty$. In this situation, a perturbation approach to solving (D3) (Smith & Bodonyi 1982) establishes that

$$\widehat{\lambda}^+ - \widehat{\lambda}^- = \lambda_+^{(10)} \left(-A_0 \overline{c}_0 / \lambda_+^{(0)} \right)^{1/2} C^{(1)},$$

where $C^{(1)} \simeq -5.516$, from numerical computation. Thus, in the limit $\overline{\Delta} \to \infty$, the phase shift is given by

$$\phi \sim \frac{2\lambda_+^{(10)} C^{(1)}}{\overline{\alpha}_0 \left(-A_0 \lambda_+^{(0)}\right)^{3/2} \overline{c}_0^{3/2}} \left(\frac{2\lambda_+^{(10)}}{\lambda_+^{(0)2}} + \frac{1}{\lambda_+^{(0)}} \right)^{-1} \overline{\Delta}^{-3/2},$$

and this is the result used in § 4.

REFERENCES

Benney, D. J. & Bergeron, R. F. 1969 A new class of nonlinear waves in parallel flows. *Stud. Appl. Maths* **48**, 181–204.

Cowley, S. J. & Smith, F. T. 1985 On the stability of Poiseuille–Couette flow: a bifurcation from infinity. *J. Fluid Mech.* **156**, 83–100.

Drazin, P. G. 2002 *Introduction to Hydrodynamic Stability*. Cambridge University Press.

Frei, Ch., Lüscher, P. & Wintermantel, E. 2000 Thread–annular flow in vertical pipes. *J. Fluid Mech.* **410**, 185–210.

Gittler, Ph. 1993 Stability of axial Poiseuille–Couette flow between concentric cylinders. *Acta Mech.* **101**, 1–13.

Gottlieb, D., Hussaini, M. Y. & Orszag, S. A. 1984 Theory and application of spectral methods. In *Spectral methods for partial differential equations* (ed. R. G. Voigt, D. Gottlieb & M. Y. Hussaini), pp. 1–54.

Haberman, R. 1972 Critical layers in parallel flows. *Stud. Appl. Maths* **51**, 139–161.

Khorrami, M. R., Malik, M. R. & Ash, R. L. 1989 Application of spectral collocation techniques to the stability of swirling flows. *J. Comput. Phys.* **81**, 206–229.

Lin, C. C. 1955 *The Theory of Hydrodynamic Stability*. Cambridge University Press.

Mott, J. E. & Joseph, D. D. 1968 Stability of parallel flow between concentric cylinders. *Phys. Fluids* **11**, 2065–2073.

Reid, W. H. 1965 The stability of parallel flows. In *Basic Developments in Fluid Dynamics*, vol. 1 (ed. M. Holt). Academic.

Sadeghi, V. M. & Higgins, B. G. 1991 Stability of sliding Couette–Poiseuille flow in an annulus subject to axisymmetric and asymmetric disturbances. *Phys. Fluids* A **3**, 2092–2104.

Schmid, P. J. & Henningson, D. S. 2001 Stability and transition in shear flows. Springer.

Smith, F. T. 1979 Instability of flow through pipes of general cross-section. Parts I and II. *Mathematika* **26**, 187–210, 211–223.

Smith, F. T. & Bodonyi, R. J. 1982 Nonlinear critical layers and their development in streaming-flow stability. *J. Fluid Mech.* **118**, 165–185.

Stuart, J. T. 1963 Hydrodynamic stability. In *Laminar Boundary Layers* (ed. L. Rosenhead). Dover.

Walton, A. G. 2003 The nonlinear instability of thread–annular flow at high Reynolds number. *J. Fluid Mech.* **477**, 227–257.